Nano Today 62 (2025) 102735

Contents lists available at ScienceDirect

Nano Today

journal homepage: www.elsevier.com/locate/nanotoday

Nanozyme engineered ROS-tolerant cysteine active-site for upstream deubiquitylation therapy of inflammatory bowel disease

Haibin Wu [a,b,c,*,1], Shuhan Shi [a,b,1], Lenan Xu [a,b,1], Ziying Zheng [a,b], Ziyan Huang [a,b], Yi Qiu [a,b], Jixiang Zhang [a], Keyun Yang [a], Yuting Xie [a], Cheng Xu [a], Tianyang Xu [a,b], Guohuan Zeng [a], Lingfeng Chen [a,b], Mincong Huang [a], Qian Chen [d,**], Daishun Ling [e,**], Guang Liang [a,b,c,*]

[a] School of Pharmaceutical Sciences, Hangzhou Medical College, Hangzhou 311399, Zhejiang, China
[b] Department of Pharmacy and Institute of Inflammation, Zhejiang Provincial People's Hospital, Affiliated People's Hospital, Hangzhou Medical College, Hangzhou 310014, Zhejiang, China
[c] Affiliated Lin'An People's Hospital, Hangzhou Medical College, Hangzhou, Zhejiang 311399, China
[d] State Key Laboratory of Chinese Medicine Modernization, Innovation Center of Yangtze River Delta, Zhejiang University, Jiaxing, Zhejiang 314102, China
[e] Frontiers Science Center for Transformative Molecules, School of Chemistry and Chemical Engineering, School of Biomedical Engineering, National Center for Translational Medicine, Shanghai Advanced Research Institute, Shanghai Jiao Tong University, Shanghai 200240, China

ARTICLE INFO

Keywords:
Nanozyme
Cysteine active-site
Deubiquitylation therapy
Upstream anti-inflammatory therapy
Inflammatory bowel disease

ABSTRACT

Deubiquitinase (DUB)-based upstream regulation of inflammatory pathway has emerged as a promising strategy for inflammatory bowel disease (IBD) compared to clinical biological therapies that block downstream inflammatory mediators. Unfortunately, excessive reactive oxygen species (ROS) in the inflammatory microenvironment usually induces irreversible oxidation of the cysteine active-site of therapeutic DUB, resulting in the rapid fading of deubiquitylation activity and inferior anti-inflammatory efficacy. Herein, a redox active nanozyme boosted deubiquitylation strategy based on the natural-artificial dual catalytic nanodrug (NADCN) is designed for protecting the vulnerable catalytic active center of anti-inflammatory DUB. Benefiting from the nanozyme-enabled protection of DUB's cysteine active-site, the NADCN exhibits far superior anti-inflammatory activity to that of its counterparts based on the conventional delivery system. Moreover, the redox nanozyme in NADCN confers efficient modulation of the oxidative and hypoxia inflammatory microenvironment, further unleashing the potential of DUB for treatment of IBD. Therefore, the NADCN opens a new avenue to protect the cysteine active-site of therapeutic DUB, providing an attractive opportunity for developing ROS-tolerant deubiquitylation therapy.

Introduction

Inflammatory bowel disease (IBD) is a chronic disorder of the gastrointestinal tract that influence millions of people worldwide, which often occurs in young and middle-aged patients [1–4]. The symptoms of IBD, such as diarrhea, abdominal pain, fatigue, rectal bleeding, weight loss, depression and increased risk of bowel cancer can severely compromise patients' quality of life [5,6]. Although the exact underlying etiologies are still poorly understood, extensive studies have shown that dysregulated immune haemostasis plays a crucial role in the pathogenesis of IBD [7]. Therefore, immunosuppressive and anti-inflammatory drugs are widely used for the clinical treatment of IBD, which however, generally target the downstream inflammatory mediators, such as tumor necrosis factor-α (TNF-α), IL-6 [7]. As a result, these anti-inflammatory drugs usually require high-dose, high-frequency administration [8–10], which are frequently confronted with severe side effects such as bone marrow suppression, nephrotoxicity, hepatotoxicity, and drug resistance [9,10]. Moreover, poor adherence and injection anxiety of patients to these high-dose, high-frequency anti-inflammatory drugs can also lead to treatment failure [8–10]. These

* Corresponding authors at: School of Pharmaceutical Sciences, Hangzhou Medical College, Hangzhou 311399, Zhejiang, China.
** Corresponding authors.
E-mail addresses: wuhaibin@hmc.edu.cn (H. Wu), chenqian08@zju.edu.cn (Q. Chen), dsling@sjtu.edu.cn (D. Ling), wzmcliangguang@163.com (G. Liang).
[1] These authors contributed equally to this work.

https://doi.org/10.1016/j.nantod.2025.102735
Received 23 November 2024; Received in revised form 1 March 2025; Accepted 20 March 2025
Available online 28 March 2025

results indicate that targeting the downstream cytokines of inflammatory pathways maybe not sufficient for combating IBD [9,10]. Hence, modulation of the upstream signals underlying inflammatory response for the treatment of IBD would be a desirable and efficient strategy, but is rarely developed.

Deubiquitinase (DUB) is a family of protease that remove ubiquitin from protein substrates, which are essential to various cellular processes [11]. Although current research mainly focuses on its role in intracellular protein homeostasis, the biomedical applications of DUB have also attracted increasing attentions recently. For example, several studies demonstrated the great therapeutic potential of DUBs in the treatment of osteoporosis and cardiac hypertrophy, which may provide new insights for the treatment of IBD [12,13]. Indeed, recent studies have revealed that post-translational modification of proteins by DUB plays a crucial role in regulating the upstream mediators of inflammation response in IBD [14–16]. For example, Zhang et al. demonstrated that ovarian tumor deubiquitinase 1 (OTUD1) with a cysteine active-site could efficiently suppress the IBD-related colonic inflammation by cleaving the K63 ubiquitin chain from receptor-interacting serine/threonine-protein kinase 1 (RIPK1) [17], which is the upstream mediator of typical NF-κB inflammatory signalling. Moreover, Dean et al. also found that the cysteine DUB cezanne could suppress NF-κB activation by cleaving ubiquitin chain from the upstream regulator [18]. Given the emerging evidences showing the therapeutic effectiveness of DUB and superiority of upstream anti-inflammatory strategy, it is reasonable to consider DUB as promising alternatives for IBD treatment. However, the majority of DUB, including OTUD1 and cezanne, belong to the cysteine protease class, whose biological activities greatly depend on the thiol group (-SH) of the active-site cysteine residues [19,20]. Unfortunately, the inflamed colon tissues of IBD patients usually generate excessive amounts of reactive oxygen species (ROS) [21,22], which can directly oxidize the cysteine active-site of DUB and induce the loss of enzymatic activity. Therefore, the clinical translation of deubiquitylation therapy for IBD has been significantly hampered by the poor stability of the vulnerable cysteine residues of DUB in inflamed colon tissues. A therapeutic strategy that can efficiently protect the vulnerable cysteine active-site in DUB is highly crucial and desired for the deubiquitylation therapy of IBD.

Recently, nanozymes have attracted intensive attention and achieved excellent performance in various biomedical field owing to their desirable biological characteristics and unique catalytic properties [23–26]. Among these nanozymes, platinum nanozyme (PtNZ) with both the catalase (CAT)-mimetic and superoxide dismutase (SOD)-mimetic properties has been identified as a promising nanozyme for the elimination of excessive ROS in inflammatory tissues [27]. Additionally, studies have shown that nanozymes can enhance the stability and penetration capacity of drugs [28,29], thus making them optimal choices for engineering highly efficient drug delivery system and enhancing drug therapeutic effects. In this work, we report a nanozyme boosted deubiquitylation strategy to protect the vulnerable cysteine active-site in anti-inflammatory DUB OTUD1 (Scheme 1). Specifically, the ROS-scavenging PtNZ and the anti-inflammatory OTUD1 are co-assembled into the nanosized zeolitic imidazolate framework-8

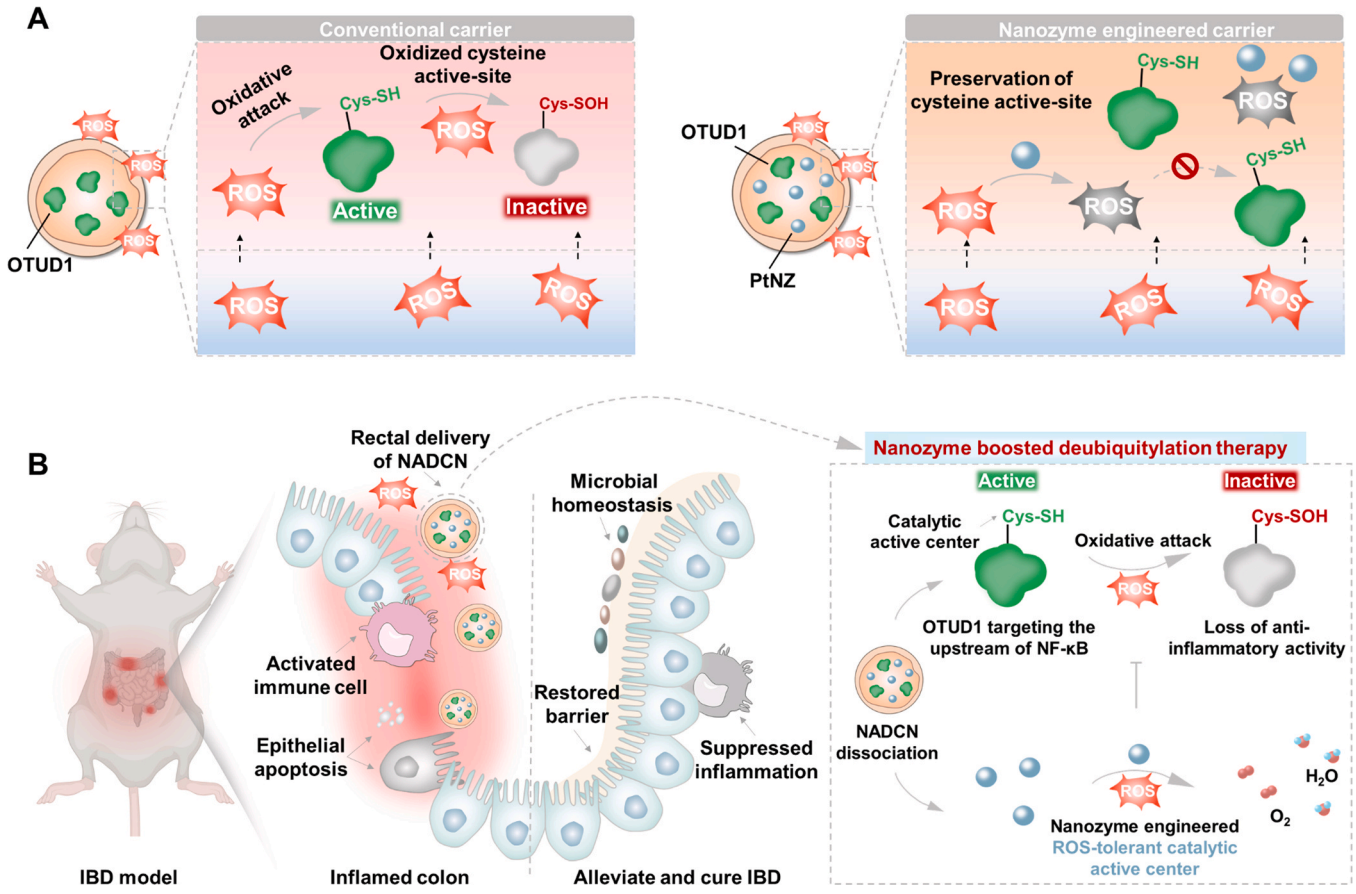

Scheme 1. Design and fabrication of the NADCN for nanozyme boosted deubiquitylation therapy of IBD. (A) Schematic illustration showing the comparison of deubiquitylation therapy via the nanozyme engineered NADCN and conventional delivery system. (B) Schematic illustration of the IBD treatment mechanisms by NADCN. After accumulating in the mucus layer, the encapsulated PtNZ with SOD/CAT-mimetic activities could scavenge overexpressed ROS in the inflamed colon to generate O_2, thus reshaping the hostile oxidative and hypoxia inflammatory microenvironment. Furthermore, the integrated PtNZ could prevent detrimental oxidation of the cysteine active-site in the deubiquitinating enzyme OTUD1, resulting in efficient suppression of inflammatory response and proinflammatory cytokine secretion. The cooperative coupling of hostile inflammatory microenvironment modulation with upstream suppression of NF-κB pathway by NADCN leads to effective treatment of IBD.

(ZIF-8) to construct the natural-artificial dual catalytic nanodrug (NADCN) for ROS-tolerant deubiquitylation therapy of IBD. The integrated nanozyme endows the anti-inflammatory OTUD1 with ROS-tolerant catalytic active center in the highly hostile inflammatory microenvironment with excessive ROS, thus maintaining the OTUD1's bioactivity to enable effective upstream inhibition of NF-κB pathway. Nevertheless, efficient modulation of the oxidative and hypoxia inflammatory microenvironment in IBD is also achieved by the NADCN, further improving the anti-inflammatory effect of OTUD1. Interestingly, the CAT-mimetic activity of integrated PtNZ confers the NADCN with photoacoustic imaging-guided deubiquitylation therapy of IBD by the catalytic bubble-triggered inertial cavitation mechanism [30]. To the best of our knowledge, this is the first strategy in which the inorganic nanozyme is integrated to engineer ROS-tolerant catalytic active center for natural DUB, which hold great promise for ROS-tolerant and imaging-guided deubiquitylation therapy of IBD.

Results and discussion

Fabrication and structural characterization of NADCN

In the present study, we designed a natural-artificial dual catalytic nanodrug NADCN to engineer ROS-tolerant catalytic active center for boosted deubiquitylation therapy of IBD. The synthetic approach for NADCN is illustrated in Fig. 1A. In brief, ultra-small and uniformly dispersed polyvinylpyrrolidone (PVP)-stabilized PtNZ with a diameter about 2 nm is first synthesized via the chemical reduction of Pt precursor with $NaBH_4$ (Fig. 1B). As illustrated in Figure S1, the PtNZ exhibits impressive superoxide dismutase (SOD)- and catalase (CAT)-mimetic activities by efficiently eliminating the ROS, such as superoxide ($\bullet O_2^-$) and hydrogen peroxide (H_2O_2), thus suitable for constructing nanozyme-empowered OTUD1 delivery system. After expression in *Escherichia coli* and further purification by gel filtration chromatography, the molecular weight and deubiquitylation activity of natural DUB enzyme OTUD1 were detected using sodium dodecyl sulfate-polyacrylamide gel electrophoresis (SDS-PAGE) analysis and ubiquitin-7-amido-4-methylcoumarin (Ub-AMC) assay, respectively (Figure S2). In order to guarantee the structure stability and loading efficacy, OTUD1 enzyme encapsulation requires mild reaction conditions and porous carrier. Specifically, ZIF-8 with a porous structure is ideal for protein encapsulation and delivery. Notably, ZIF-8 can be synthesised under room temperature or even 4 °C in pure aqueous condition without using hydrophobic solution, which is beneficial for maintaining the stability and activity of biological cargos. Therefore, ZIF-8 is chosen as the nanoplatform for construction of NADCN. Upon demonstrating the redox regulation capacity of PtNZ, an enzyme compatible co-assembly approach is adopted to construct NADCN by simultaneously encapsulating the OTUD1 and PtNZ into the ZIF-8 scaffold. Initially, the OTUD1 protein and PtNZ may form pre-nucleated clusters with ZIF-8 precursors via the electrostatic interaction or hydrogen bond [31]. Subsequently, these clusters could serve as the core for ZIF-8 growth and the formation of OTUD1-PtNZ loaded NADCN.

To verify the incorporation of PtNZ into the ZIF-8 matrix, the resulting NADCN is next characterized by transmission electron microscopy (TEM). Since the PtNZ plays a crucial role in preserving the bioactivity of OTUD1, the PtNZ/OTUD1 feed ratio should be optimized to simultaneously offer appropriate encapsulation efficiency and optimal anti-inflammatory performance. Therefore, we first investigate the

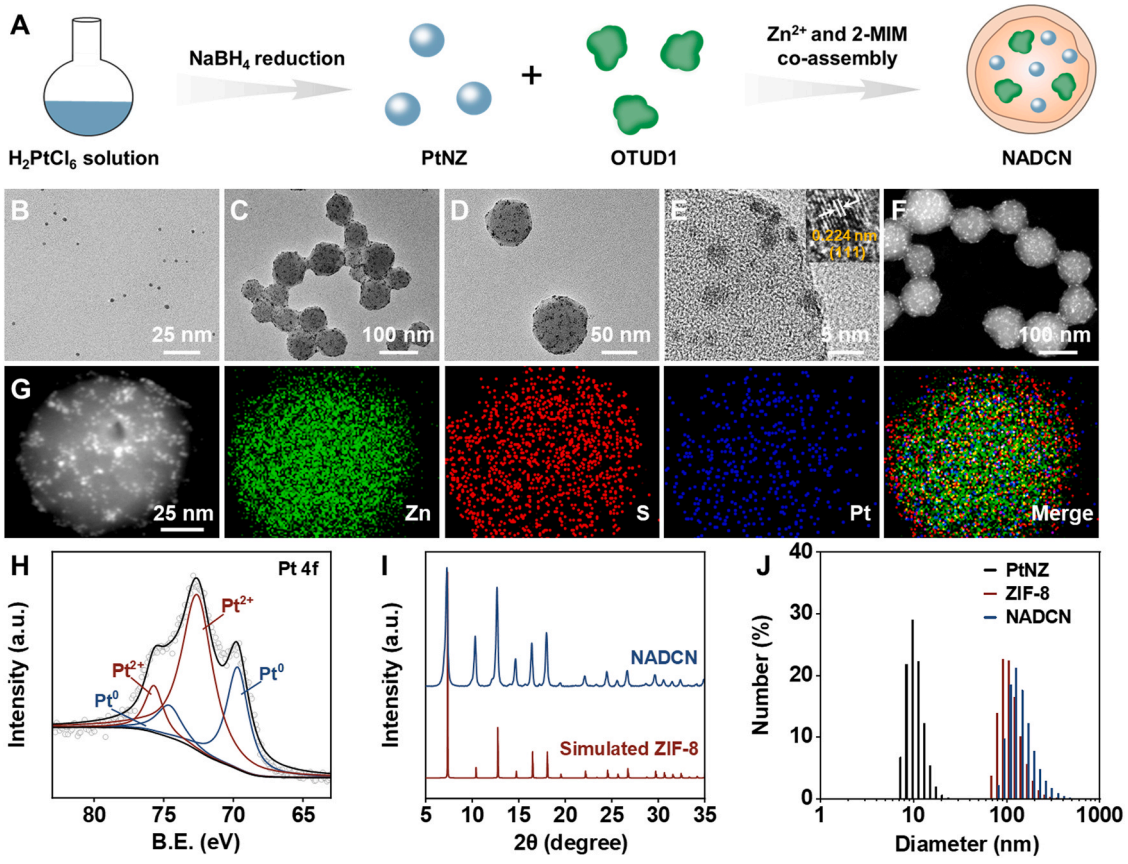

Fig. 1. Preparation and structural characterization of NADCN. (A) Schematic illustration of the synthetic approach for NADCN. (B) TEM image of the PtNZ. (C) TEM image of the NADCN. (D) The corresponding enlarged TEM of NADCN. (E) The HRTEM image of NADCN, inset is the crystallographic lattice fringes of incorporated PtNZ in NADCN. (F) The STEM image of the NADCN. (G) HAADF-STEM image and the corresponding EDX mapping (Zn, S, and Pt) images of the NADCN. (H) High-resolution XPS spectra of *Pt 4 f* in NADCN. (I) XRD pattern of the NADCN. (J) DLS characterization of PtNZ, ZIF-8, and NADCN.

effects of PtNZ/OTUD1 feed ratio on the encapsulation efficiency. As shown in Figure S3, Supporting Information, a complete encapsulation of PtNZ occurs when the PtNZ/OTUD1 feed ratio is 5:1 or less during the fabrication process. Moreover, the improvement of the NADCN's anti-inflammatory performance reaches its peak when the PtNZ/OTUD1 feed ratio is 5:1 (Figure S4, Supporting Information). Therefore, the 5:1 PtNZ/OTUD1 feed ratio is chosen for fabricating NADCN and subsequent biological application research. As shown in Fig. 1C, D, PtNZ is evenly distributed throughout the NADCN. Besides, Pt crystallographic lattice fringes in the high-resolution TEM (HRTEM) image of NADCN also confirm the efficient encapsulation of PtNZ (Fig. 1E). Meanwhile, to determine whether the OTUD1 is encapsulated in NADCN, OTUD1 is labelled with fluorescein isothiocyanate (FITC) for observation. As shown in Figure S5, the fluorescently labelled OTUD1 is primarily located in the sediment rather than supernatant after the co-assembly process, suggesting that the OTUD1 is incorporated into the NADCN nanoformulation and can be separated via centrifugation. In contrast, the free FITC-OTUD1 protein remains the solution state after centrifugation. As shown by the isolated bright spots originated from the high Z-contrast PtNZ, high-angle annular dark-field scanning transmission electron microscopy (HAADF-STEM) further confirms the incorporation of PtNZ into NADCN (Fig. 1F). Moreover, corresponding energy-dispersive X-ray (EDX) elemental mapping results also indicate that Zn (from ZIF-8), S (from OTUD1), and Pt (from PtNZ) elements are uniformly distributed in NADCN (Fig. 1G), indicating both PtNZ and OTUD1 protein are successfully introduced into the ZIF-8 structure. Next, NADCN is characterized by X-ray photoelectron spectroscopy (XPS) to investigate the valence state and composition of NADCN. As shown in Figure S6, XPS spectrum also confirms the existence of the Zn, S, and Pt element in NADCN. Notably, the high-resolution *Pt 4 f* XPS spectrum exhibits two pairs of peaks assigned to Pt^0 and Pt^{2+}, implying that the valence state of Pt is between 0 and + 2 (Fig. 1H). X-ray diffraction (XRD) pattern reveals that NADCN match well the simulated data of ZIF-8, indicating the protein and nanozyme encapsulation has negligible effect on the crystalline structure of NADCN (Fig. 1I). Dynamic light scattering (DLS) data reveals the excellent particle dispersion of NADCN in water (Fig. 1J). Moreover, we further investigate the stability of NADCN in PBS and simulated colon fluids (SCF). DLS measurements display no obvious changes in the hydrated size, confirming the NADCN exhibits good stability in these physiological solutions (Figure S7, Supporting Information). However, the NADCN decomposes into fragments after incubation in acid condition that mimic the

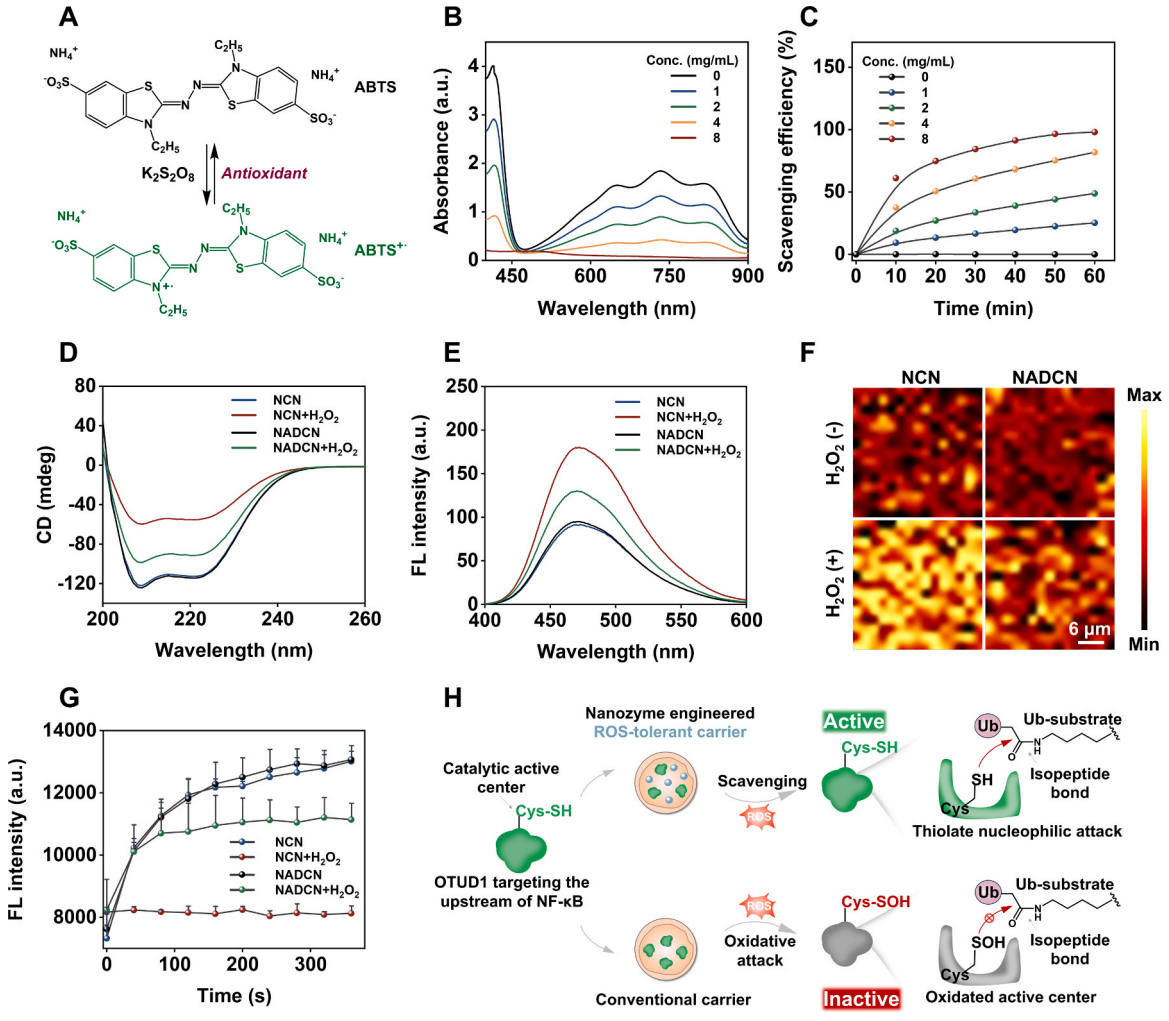

Fig. 2. NADCN maintains the activity of OTUD1 by protecting -SH catalytic active center. (A) The generation and elimination mechanisms of $ABTS^{+\bullet}$ radicals. (B) Ultraviolet-visible (UV–vis) spectra of $ABTS^{+\bullet}$ radicals treated with different concentration of NADCN at 60 min. (C) In vitro scavenging efficiency of $ABTS^{+\bullet}$ radicals recorded from 0 to 60 min with different concentrations of NADCN. Data are shown as mean ± S.D. (n = 4). (D) CD spectra of NCN or NADCN before and after the H_2O_2 treatment. (E) ANS fluorescence spectra of NCN or NADCN with or without exposure to H_2O_2. (F) Representative Raman mapping images around 820 cm^{-1} corresponds to the S═O/S-O group of NCN or NADCN before and after the H_2O_2 treatment. (G) Ub-AMC assay for OTUD1 of NCN and NADCN with or without exposure to H_2O_2. Data are shown as mean ± S.D. (n = 3). (H) Schematic illustration of NADCN-enabled ROS-tolerant catalytic active center for boosted deubiquitylation activity in the mimetic oxidative microenvironment.

inflammatory microenvironment, indicating a pH-responsive collapse and release behavior of NADCN (Figure S8, Supporting Information). Therefore, the NADCN could keep stable under physiological conditions and degrade under acid condition (Figure S7 and S8, Supporting Information). According to the above results, it is reasonable to conclude that the NADCN is successfully constructed.

Nanozyme-enabled ROS-tolerant deubiquitylation activity

Having confirmed the successful fabrication and detailed composition of NADCN, we next test whether the nanoformulation can resist the ROS-induced oxidative damaging of encapsulated OTUD1 protein. The overall antioxidant capacity of NADCN is firstly investigated via the classical 2,2′-azino-bis(3-ethylbenzothiazoline-6-sulfonic acid) radical ($ABTS^{+\bullet}$) assay, where the dark blue $ABTS^{+\bullet}$ radicals can be reduced to colorless ABTS in the presence of antioxidants. As shown in Fig. 2A-C, the NADCN treatment leads to an obvious decrease in the absorption of $ABTS^{+\bullet}$ at 734 nm, suggesting that the antioxidant activity of PtNZ is well preserved after the incorporation process. Subsequently, the secondary structure evolution of the encapsulated OTUD1 protein before and after H_2O_2 treatment is investigated by circular dichroism (CD) [32]. For comparison, the OTUD1 incorporated natural catalytic nanodrug (NCN) without PtNZ is also prepared as the control to study the protective role of nanozyme. As shown in Fig. 2D, the CD spectra revealed an obvious change in the secondary structure of OTUD1 protein in the NCN group, while that of NADCN group is minimally affected after H_2O_2 treatment. Moreover, compared with the NADCN group, significant conformational changes of OTUD1 protein in the NCN group are observed by monitoring the evolution in the fluorescent intensity of the 8-anilino-1-naphthalenesulfonic acid (ANS) dye (Fig. 2E), a probe which displays increased fluorescence upon binding to exposed hydrophobic regions in proteins [33]. Hydroxyl radical (•OH) is recognized as the most reactive and toxic ROS compared to $\bullet O_2$- (superoxide radical) and H_2O_2. Therefore, the •OH is also selected to evaluate self-protective capacity of NADCN. Consistent with the H_2O_2 exposure experiments, the CD spectra and ANS results indicate that nanozyme-incorporated NADCN could effectively resist the destructive effect of •OH (Figure S9, Supporting Information), further confirming the broad-spectrum self-protective effect of NADCN.

Next, the protective efficacy of NADCN against ROS attack is investigated by a label-free and non-destructive confocal Raman imaging technique. The characteristic Raman peak around 820 cm^{-1} could be attributed to the S═O/S-O group [34], which is selected to illustrate the oxidation of -SH group in cysteine active-site. After the H_2O_2 treatment, NCN exhibits an obvious increase of S═O/S-O Raman signal, confirming the severe oxidation of the incorporated OTUD1 (Fig. 2F). However, for the nanozyme-powered NADCN, a significant lower S═O/S-O Raman signal is observed, suggesting that the crucial -SH group is well maintained during the H_2O_2 challenge process (Fig. 2F). Moreover, we also employe the thiol-reactive fluorophore Alexa-maleimide 488 (ALM-488) to precisely quantify the -SH content after various treatments. Consistent with the Raman result, the ALM-488 quantitative data indicate that the nanozyme-incorporated NADCN could effectively prevent the oxidative damage of -SH (Figure S10, Supporting Information), further validating the self-protective performance of NADCN. In addition, the fluorogenic model substrate Ub-AMC is used to further detect the in vitro deubiquitylation activity of OTUD1 [33]. Loss of deubiquitylation activity is clearly observed in the NCN group, while only a slight reduction of the deubiquitylation activity is detected in the NADCN group after the H_2O_2 treatment (Fig. 2G). Taken together, these results suggest that the NADCN could protect the OTUD1 protein from the ROS-induced oxidation, and thus, the deubiquitylation activity is well maintained in the mimetic oxidative microenvironment (Fig. 2H).

In vitro anti-inflammatory performance of NADCN

Encouraged by the excellent natural and artificial cooperative catalytic activities of the NADCN, their potential for anti-inflammatory applications is also investigated. Effective cellular internalization is a prerequisite for OTUD1 protein drug to exert their anti-inflammatory DUB effects. Then, the intracellular delivery of NADCN is studied using a commercial LysoTracker dye. As shown in Fig. 3A, compared with the free FITC-OTUD1, the green fluorescence of FITC-OTUD1 in the NADCN group overlapped well with the red signal of LysoTracker dye, implying that majority of NADCN could be efficiently internalized through endocytosis. Given that excessive ROS production and hypoxic microenvironment play an essential role on inflammatory response of IBD [35,36], the effect of NADCN on cellular ROS and oxygen level are next explored (Fig. 3B). For comparison, the PtNZ incorporated artificial catalytic nanodrug (ACN) without OTUD1 is also prepared. As shown in Fig. 3C, D, compared with lipopolysaccharide (LPS) group and NCN treatment group, the green fluorescence of the ROS indicator 2′, 7′-dichlorofluorescin diacetates (DCFH-DA) in the PtNZ-loaded ACN and NADCN group undergo a substantial decrease. Additionally, since inflammatory response can result in mitochondrial dysfunction [37], we further investigate the mitochondrial membrane potential (MMP) and mitochondrial ROS production using the MMP indicator 5,5′,6,6′-tetrachloro-1,1′,3,3′-tetraethylimidacarbocyanine iodide (JC-1) and mitochondrial specific ROS probe MitoSox, respectively (Fig. 3C, E). As shown in Fig. 3C, E, NADCN could effectively prevent mitochondrial from inflammation-related oxidative damage and maintain the normal MMP owing to their efficient ROS elimination capacity. Furthermore, the intracellular O_2 production capacity is also monitored by a O_2 quenching indicator tris (4,7-diphenyl-1,10-phenanthroline) ruthenium (II) dichloride complex ($[Ru(dpp)_3]Cl_2$), whose red fluorescence could be readily quenched by O_2. In contrast to other groups, PtNZ-contained groups (NADCN and ACN) exhibit significantly weaker fluorescence under hypoxic condition, suggesting efficient intracellular O_2 generation via the nanozyme initiated catalytic reaction (Fig. 3F, G). Meanwhile, remarkably lower hypoxia-inducible factor (HIF-1α) immunofluorescence are observed in the NADCN group, further confirming that the efficient oxygen generation mediated by the incorporated PtNZ could alleviate the hypoxic condition (Fig. 3F).

Since OTUD1 can prevent the progression of IBD by regulating the NF-κB inflammatory pathway [17], the effects of NADCN on cellular inflammatory responses are next investigated. As the data indicate that NADCN could efficiently alleviate the oxidative and hypoxic microenvironment, we are also interested in examining whether the encapsulated PtNZ can protect DUB activity of OTUD1 in the cellular level. Since p65/p50 is an essential dimerization form associated with immunity and inflammatory responses in the NF-κB protein complex, it is chosen to evaluate the activation status of the inflammatory signaling. As shown in Fig. 4A, B, NADCN treatment significantly suppressed the activation of NF-κB signaling pathway. Compared with other groups, remarkably lower expression of phosphorylated p65 (p-p65), a major NF-κB subunit, is observed in the NADCN group (Fig. 4A, B). Accordingly, the downstream inflammatory cytokine TNF-α is dramatically decreased, further suggesting the excellent anti-inflammatory activity of NADCN (Fig. 4C, D). Notably, the freeze-drying post-treatment demonstrates no significant changes on the anti-inflammatory activity of NADCN when compared to freshly prepared samples, confirming the feasibility of the freeze-drying method (Figure S11, Supporting Information). Meanwhile, the influence of NADCN on pro-inflammatory cytokines expression is also evaluated by the real-time reverse transcription polymerase chain reaction (RT-qPCR) analysis. In contrast to the NCN and ACN groups, the NADCN group exhibits significantly lower expression of pro-inflammatory cytokines, including *TNF-α*, *IL-6*, and *IL-1β* (Fig. 4E-G). Taken together, these results indicate that NADCN could effectively suppress the NF-κB inflammatory pathway and downstream pro-inflammatory cytokines (Fig. 4H).

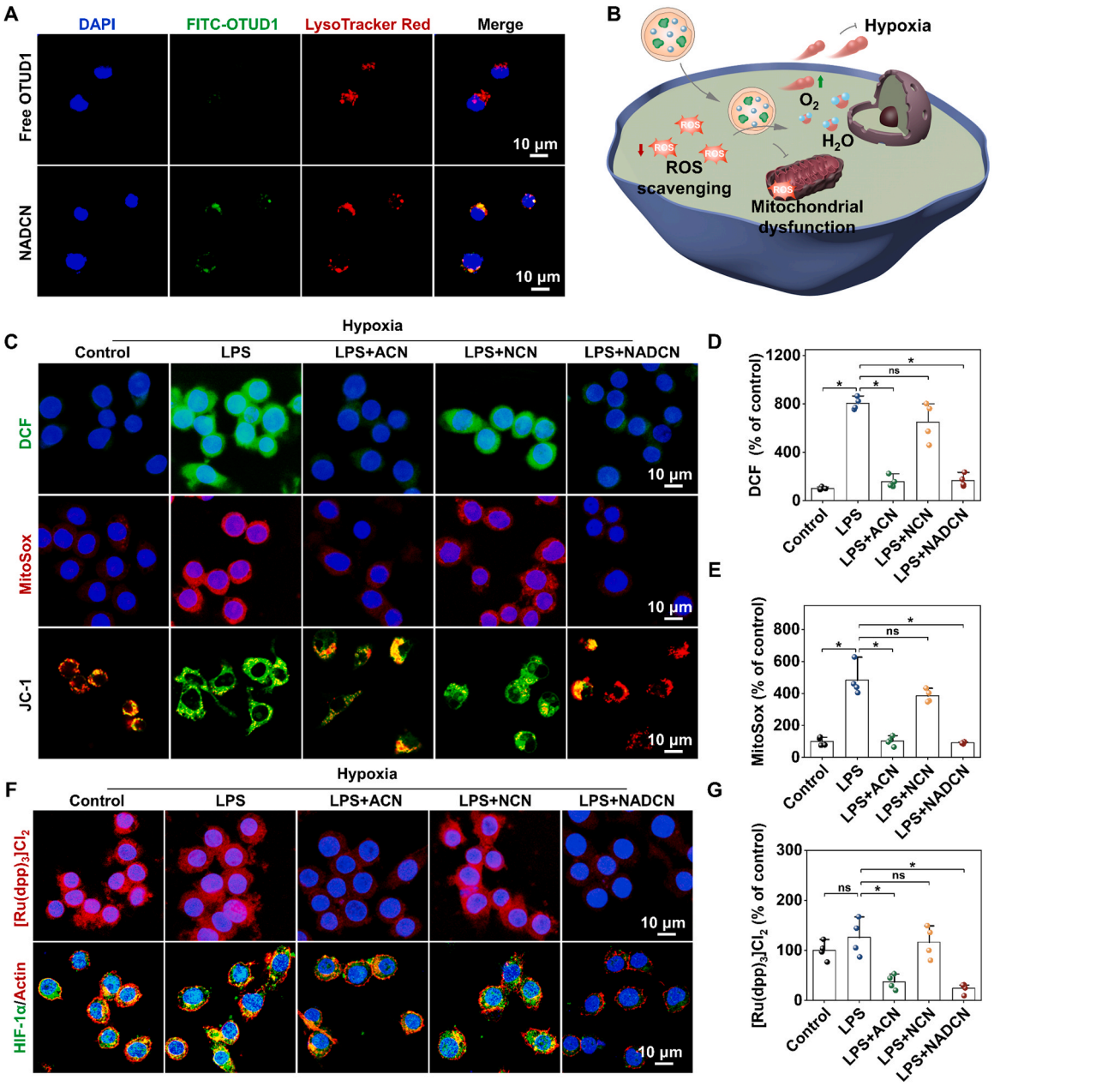

Fig. 3. NADCN-enabled alleviation of oxidative damage and hypoxia. (A) Confocal laser scanning microscopy (CLSM) images of cellular uptake of FITC-tagged free OTUD1 and NADCN, the lysosomes are stained by the LysoTracker Red dye. (B) Schematic illustration of catalytic O_2 generation and ROS elimination by NADCN. (C) CLSM images of RAW264.7 cells stained with DCFH-DA, MitoSox, or JC-1 probe following various treatments. (D) The quantified relative fluorescence intensity of the DCFH-DA with indicated treatments (n = 4). (E) Corresponding quantitative analysis of average fluorescence intensity of MitoSox staining (n = 4). (F) CLSM images of $[Ru(dpp)_3]Cl_2$ or HIF-1α stained RAW264.7 cells after different treatments. (G) Corresponding quantitative analysis of average fluorescence intensity of $[Ru(dpp)_3]Cl_2$ staining (n = 4). Data are presented as mean ± S.D. *p* values were calculated via one-way ANOVA test. $^*p < 0.05$.

Enhanced colitis mucosa retention and specific PAI of NADCN

The excellent catalytic activity and in vitro anti-inflammatory performance of NADCN motivate us to further investigate the in vivo accumulation and therapeutic effects on IBD mouse model. A major concern about DUB-based deubiquitylation therapy is the off-target effects, which may pose risks due to the unintended activation or repression of gene signaling pathways. Compared to systemic administration, localized drug delivery systems hold great promise in reducing the unwanted off-target effects. Another strategy to address the off-target issues is stimuli-responsive drug delivery platforms, as they can prevent premature release of therapeutic DUBs during delivery process. As a pH-responsive localized drug delivery platform, the NADCN offers a safe and promising approach to minimize the off-target effects of therapeutic DUBs. Therefore, the direct rectal delivery of NADCN avoids the unintended drug exposure and leakage compared to systemic administration while pH-responsive DUB release is of great potential for precise deubiquitylation therapy. To investigate the colonic retention and biodistribution of NADCN, we encapsulated a NIR fluorescent probe (indocyanine green, ICG) into the NADCN to monitor their locations through an in vivo fluorescent imaging system. Indeed, NADCN demonstrate remarkable higher fluorescence signals in the inflamed colon tissues compared to the the normal colon from healthy mice, indicating that NADCN mainly accumulate in the colitis mucosa (Fig. 5A, B). This enhanced accumulation effect of NADCN is possibly dependent on the disrupted colonic epithelial layers of the colitis

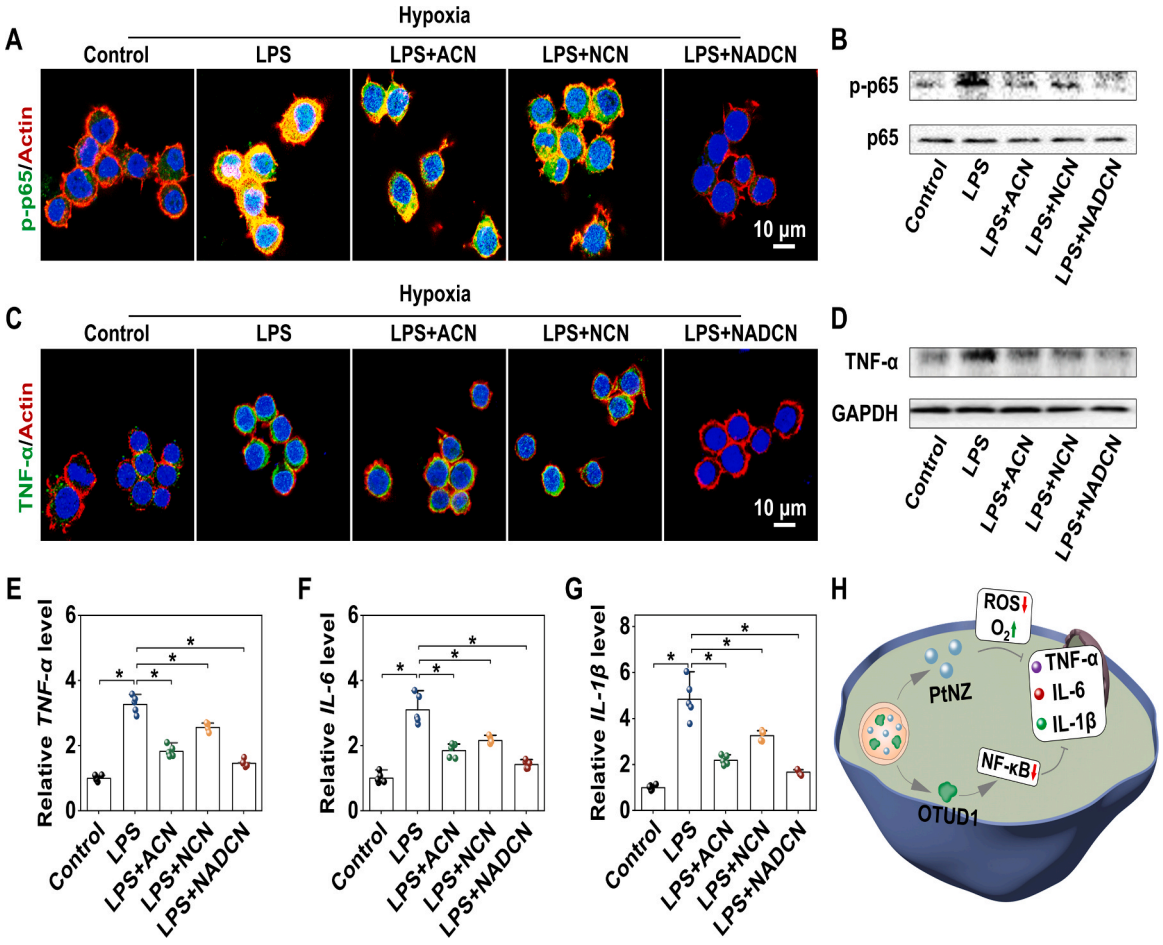

Fig. 4. Mitigation of inflammatory process by NADCN. (A) CLSM images of RAW264.7 cells immuno-stained with p-p65 after various treatments (p-p65, green channel; Nuclei, DAPI channel, blue; Actin, phalloidin-Alexa Fluor 555, red channel). (B) Western blotting analysis of p-p65 protein expression with indicated treatments. (C) CLSM images of RAW264.7 cells immuno-stained with TNF-α following various treatments (TNF-α, green channel; Nuclei, DAPI, blue channel; Actin, phalloidin-Alexa Fluor 555, red channel). (D) Western blotting analysis of TNF-α level with indicated treatments. (E-G) The gene expression levels of E) *TNF-α*, F) *IL-6*, and G) *IL-1β* in RAW264.7 cells under various conditions (n = 4). (H) Schematic illustration of the anti-inflammatory mechanism by NADCN. Data are presented as mean ± S.D. *p* values were calculated via one-way ANOVA test. $^*p < 0.05$.

mucosa [38,39]. Subsequently, the colonic mucus is stained with wheat germ agglutinin (WGA) to further confirm the in vivo accumulation and penetration of NADCN. As shown in Fig. 5C, the mucosa structures of IBD model are severely compromised and accumulation of NADCN in the IBD lesions could be clearly observed. In contrast, the healthy mice with an integrated mucosa exhibit a negligible NADCN accumulation (Fig. 5C). Further immunofluorescence studies demonstrate that NADCN mainly distributes in the CD68-overexpressed inflamed region (Fig. 5D).

Moreover, Pt-based nanomaterials also possess highly desired photoacoustic imaging (PAI) capacity [40]. As shown in Fig. 5E, the multispectral optoacoustic tomography (MSOT) signals are linearly dependent on the concentration of the PtNZ-loaded NADCN. Interestingly, the MSOT signals of NADCN also exhibit a H_2O_2-dependent enhancement, which may be attributed to the produced O_2 microbubbles during the CAT-mimetic decomposition of H_2O_2 by NADCN (Fig. 5F). Therefore, specific PAI of the H_2O_2 overexpressed inflamed colonic tissue could be achieved through the O_2 microbubbles-enabled inertial cavitation mechanism with assistance of PtNZ-loaded NADCN [30]. As expected, the photoacoustic signals of NADCN in the ROS-overexpressed inflamed colon are dramatically higher than that of the healthy colon (Fig. 5G, H), revealing a promising potential on accurate diagnosis of IBD lesions and PAI-guided precise therapy (Fig. 5I).

Therapeutic efficacy and anti-inflammatory mechanisms of NADCN against DSS-induced colitis

Having confirmed the nanozyme-enabled protection of anti-inflammatory OTUD1 and enhanced colitis mucosa retention, we next evaluate the therapeutic efficacy of NADCN in a DSS-induced acute colitis murine model (Fig. 6A). As shown in Fig. 6B, mice after DSS exposure exhibit remarkable rectal bleeding, a typical hallmark of acute colitis. Notably, compared with other treatments, the symptoms of rectal bleeding are effectively mitigated by the NADCN treatment (Fig. 6B). Furthermore, endoscopic examinations indicate that the colon in the NADCN group exhibit a well-preserved smooth and intact mucosal layer similar to the normal colon of healthy mice (Fig. 6B). We next evaluate the efficacy of NADCN by monitoring the changes in disease activity index (DAI), body weight, and colon length. Consistently, the NADCN group exhibits a decreased DAI score, limited weight loss, and prolonged colon length as compared to the ACN or NCN group, further demonstrating the cooperative therapeutic efficacy of NADCN against DSS-induced colitis (Fig. 6C-F). To gain a deep insight into the therapeutic effects of NADCN, the histopathological changes in the colon tissues are next evaluated. According to the hematoxylin and eosin (H&E) staining, obvious inflammatory cell infiltration and severe crypt damage are observed in the colon tissue of the colitis mice, while treatment with NADCN could effectively reverse DSS-induced colon damage and restore the crypt and mucosal layer structure (Fig. 6G, H). Besides, as indicated

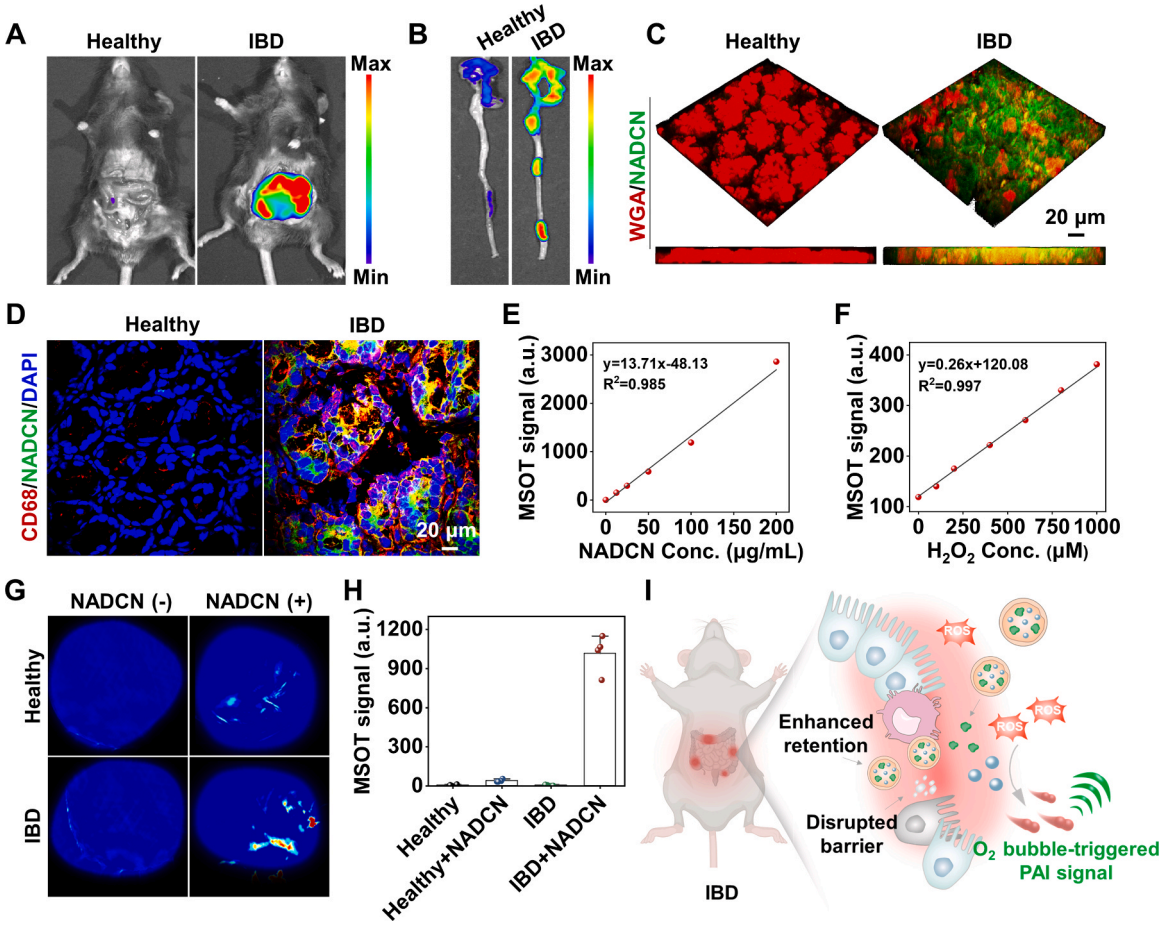

Fig. 5. Enhanced colitis mucosa retention and specific PAI of NADCN. (A) In vivo fluorescence images of colon tissues from healthy mice or dextran sulfate sodium (DSS)-induced colitis mice after rectal administration of the ICG-labelled NADCN. (B) Ex vivo fluorescence images of ICG-labelled NADCN from colon tissue of healthy mice or DSS-induced colitis mice after rectal administration. (C) 3D CLSM images of the colonic mucus stained with iFluor 647-conjugated WGA from FITC-NADCN treated healthy mice or DSS-induced colitis mice (FITC-NADCN, green channel; WGA, iFluor 647, red channel). (D) CLSM images of colonic tissues immunostained with CD68 from FITC-NADCN treated healthy mice or DSS-induced colitis mice (FITC-NADCN, green channel; Nuclei, DAPI, blue channel; CD68, red channel). (E) Concentration-dependent photoacoustic signals of NADCN. (F) Quantitative analysis of photoacoustic signals of NADCN at different concentrations of H_2O_2. (G) In vivo PA images and (H) quantitative data of healthy mice or DSS-induced colitis mice in the presence or absence of NADCN. Data are presented as mean ± S.D. (n = 4). (I) Schematic illustration of enhanced accumulation and specific PAI of NADCN in the disrupted and inflamed colitis mucosa.

by the Alcian blue-periodic acid Schiff (AB-PAS) staining, the mucus-secreting goblet cells, an important type of cell for the epithelial barrier homeostasis, are significantly elevated in the NADCN group as compared to the other treatment groups (Fig. 6I). Meanwhile, immunofluorescence staining and corresponding quantitative analysis reveal that the level of tight junction proteins, including Zonula Occluden-1 (ZO-1), Claudin-1, and Occludin-1, are significantly elevated in the colon tissues of NADCN group, further verifying the restoration of mucosal barrier function by NADCN (Fig. 6K-L and Figure S12). In addition, the serum fluorescence intensity of FITC-dextran 4 kDa (FD-4), an intestinal permeability marker, in the NADCN group decrease significantly as compared to the other treatment groups, proving the restored structural compactness of the mucosal barrier after NADCN treatment (Figure S13). Notably, as indicated by the decreased spleen weight and spleen index, NADCN could effectively alleviate the in vivo immune response, possibly owing to the restored mucosal barrier prevent the invasion of heterogeneous antigens (Figure S14).

Next, we seek to clarify the underlying mechanism of the excellent therapeutic efficacy against colitis by NADCN. The modulation effect of different treatments on the oxidative and hypoxic inflammatory microenvironment is evaluated by the immunofluorescence analysis. As shown in Fig. 7A, 8-hydroxy-2′-deoxyguanosine (8-OHdG) and 4-hydroxynonenal (4-HNE) staining of the colonic tissues for oxidative product detection suggest that colonic tissues of DSS-induced colitis mice suffer excessive oxidative stress and oxidative damage, which could be effectively mitigated by the NADCN treatment. Meanwhile, as verified by immunofluorescence staining of hypoxia-inducible factors-1α (HIF-1α), colonic tissues of the DSS-induced colitis mice exhibit a severe hypoxic state (Fig. 7A). By comparison, considerable alleviation of the colonic tissue hypoxia is achieved by NADCN (Fig. 7A). Consistently, the level of malondialdehyde (MDA) and carbonylated protein, byproducts of oxidative damage, are also significantly lower than that in the ACN, NCN, and IBD groups (Figs. 7B and 7C). Taken together, these data highlight the excellent activities of NADCN in reshaping the hostile oxidative and hypoxic microenvironment, holding great potential to protect and deliver the fragile OTUD1 protein drugs into IBD lesions.

Generally, the NF-κB signaling pathway has been confirmed to play a crucial role on the pathogenesis of IBD through the downstream pro-inflammatory cytokines (TNF-α, IL-6, and IL-1β). As shown in Fig. 7D, the TNF-α level in the DSS-induced colitis mice is much higher than the healthy mice, demonstrating the severe inflammation in IBD lesions. In contrast, obvious decrease of TNF-α is observed in the NADCN group, indicating the excellent anti-inflammation capacity of NADCN (Fig. 7D). Notably, the NCN group loaded with OTUD1 protein drug only exhibits moderate anti-inflammation effect, which may attribute to the minimal anti-inflammatory biological activity and inferior stability of OTUD1 in

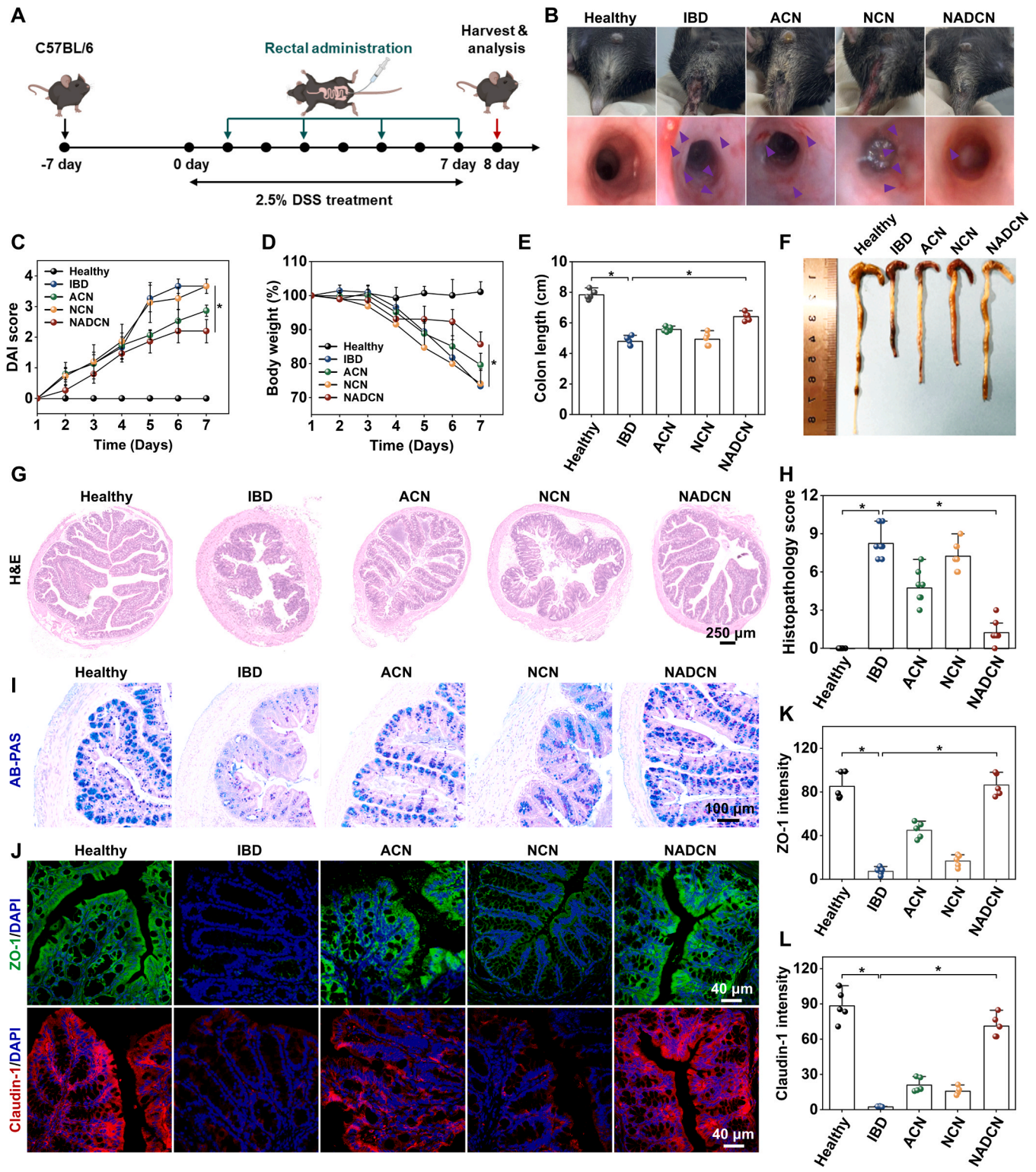

Fig. 6. Therapeutic efficacy and restoration of barrier function by NADCN. (A) Experimental flow of the animal study. (B) Representative photographs of rectal bleeding and mini-endoscopic images of colons in mice following indicated treatments. (C) Evolution of DAI score in each group with indicated treatments (n = 5). (D) Daily changes of body weight in each group after indicated treatments (n = 5). (E) The length and (F) representative photographs of colon tissues following indicated treatments (n = 5). (G) Representative H&E images and (H) corresponding histopathology scores of colon tissues following indicated treatments (n = 8). (I) Representative AB-PAS images of the colon tissues after indicated treatments. (J) Immunofluorescence staining of ZO-1 and Claudin-1 in the colon tissues of each group. Quantitative analysis of the (K) ZO-1 and (L) Claudin-1 level in the colon tissues of each group (n = 5). Data are represented as mean ± S.D. *p* values were calculated via Mann-Whitney U-test in C and D, and one-way ANOVA test in E, H, K and L. $^{*}p < 0.05$.

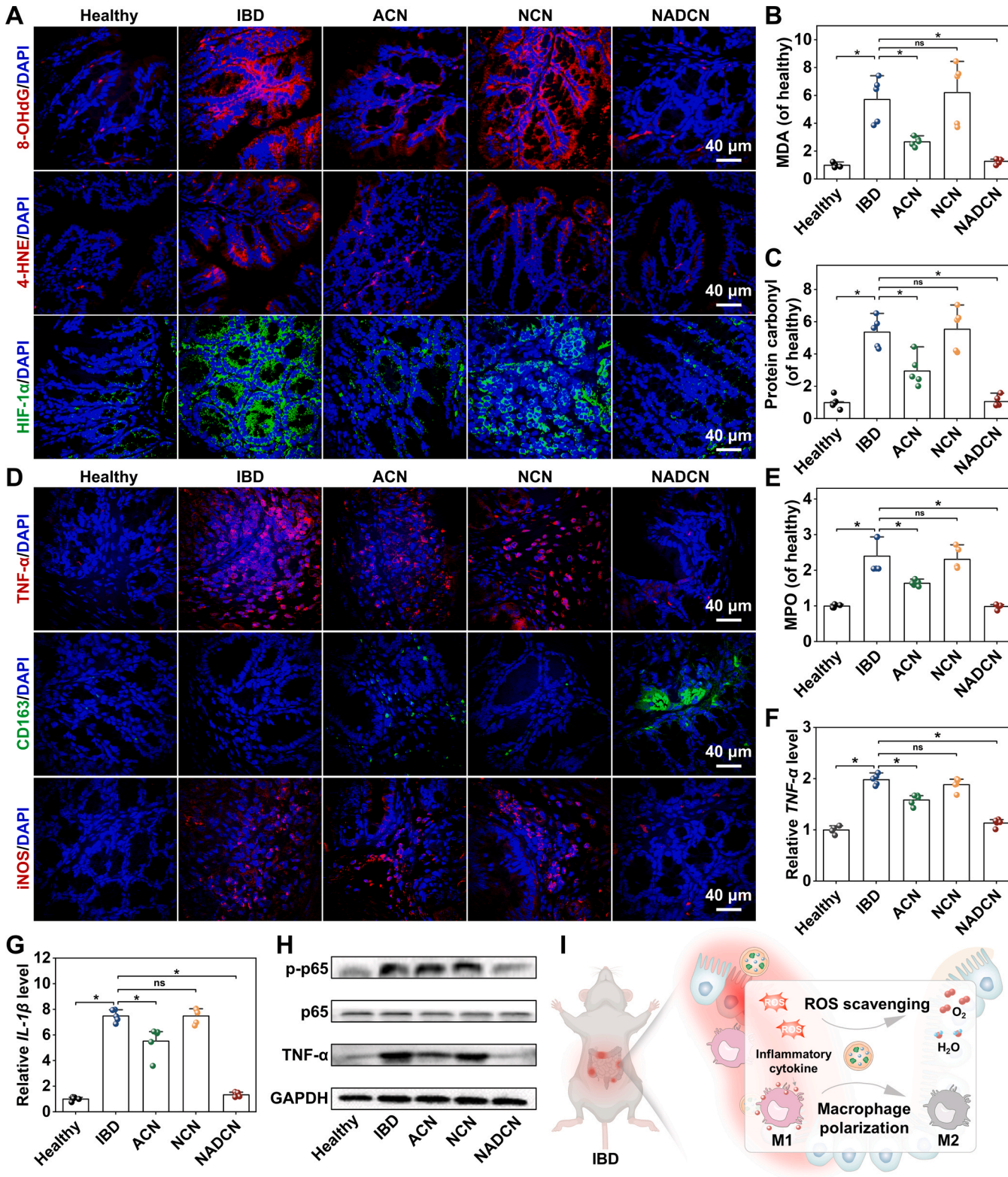

Fig. 7. Regulation of the colitis immunity by NADCN. (A) 8-OHdG (biomarker of oxidative DNA damage), 4-HNE (biomarker of lipid peroxidation), and HIF-1α (biomarker of tissue hypoxia) immunofluorescence staining of the colon tissues of healthy and different IBD treatment groups. (B) Relative level of MDA in the colon tissues of healthy and different IBD treatment groups (n = 5). (C) Relative level of carbonylated protein in the colon tissues of healthy and different IBD treatment groups (n = 5). (D) Immunofluorescence staining for TNF-α, CD163 (biomarker of M2 macrophages), and iNOS (biomarker of M1 macrophages) of the colon tissues from healthy and different IBD treatment groups. (E) Relative level of MPO in the colon tissues of healthy and different IBD treatment groups (n = 5). RT-qPCR analysis of F) *TNF-α* and G) *IL-1β* mRNA expression in the colon tissues of healthy and different IBD treatment groups (n = 5). (H) WB analysis of the p-p65, p65, and TNF-α protein level in the colon tissues of healthy and different IBD treatment groups. (I) Schematic illustration of the synergistic anti-inflammatory efficacy of NADCN against DSS-induced colitis. Data are presented as mean ± S.D. *p* values were calculated via one-way ANOVA test. *$p < 0.05$.

the hostile oxidative and hypoxic microenvironment (Fig. 7D). To elucidate the evolution of immune microenvironment in IBD lesions, we also investigate the infiltrated immune cells and disclosure the phenotypes of immune cells through the immunofluorescence staining for iNOS (a marker of proinflammatory M1 macrophages) and CD163 (a marker of anti-inflammatory M2 macrophages) [41,42]. In contrast to other treatment groups, NADCN treatment effectively promotes the polarization of infiltrated macrophages toward anti-inflammatory M2 phenotypes, thus greatly favoring the inflammation resolution and tissue hemostasis of colitis tissues (Fig. 7D). In addition to the desirable macrophage polarization effect, the colonic myeloperoxidase (MPO) activity, an important neutrophil infiltration marker [43], in NADCN

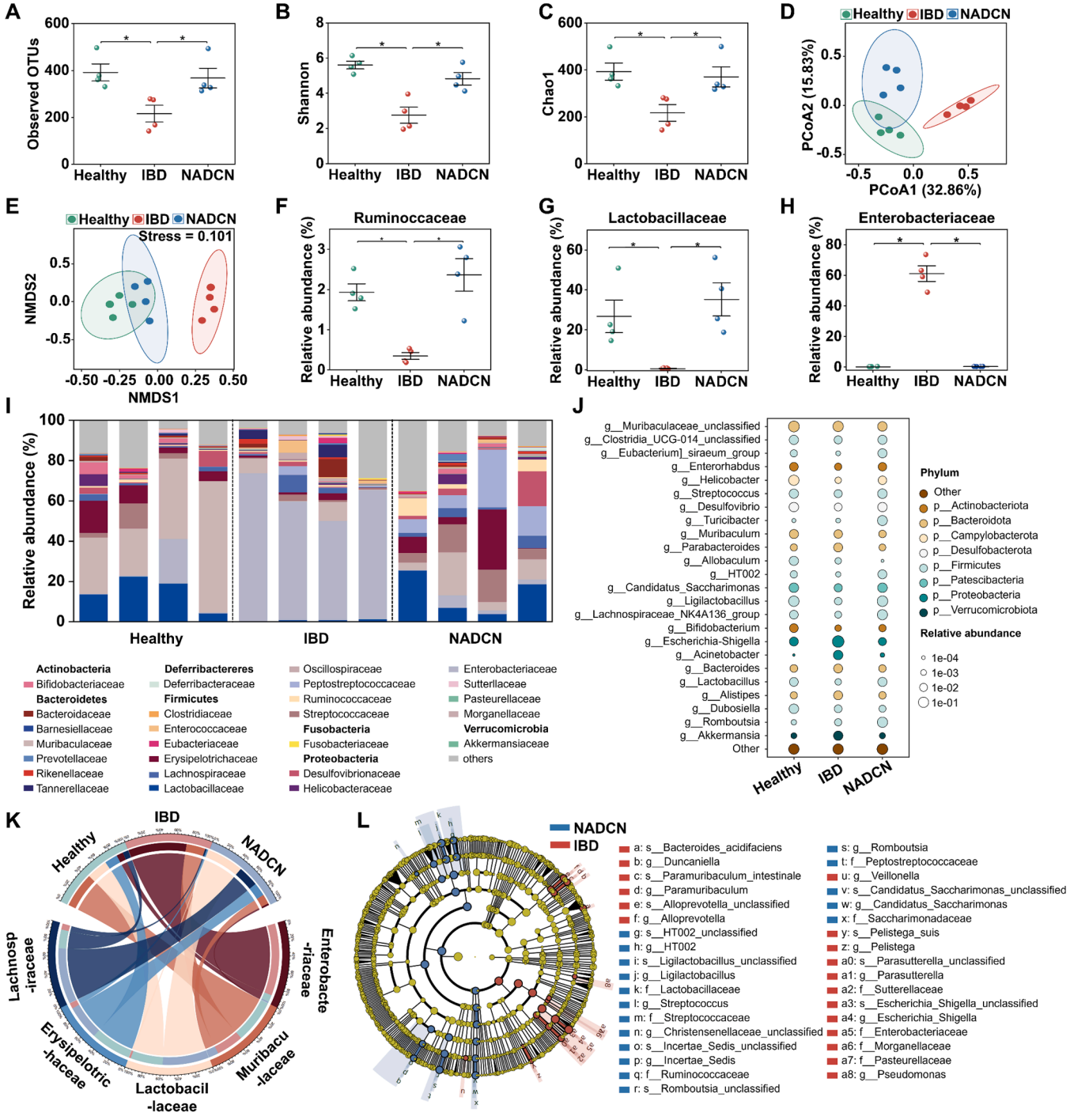

Fig. 8. Modulation of gut microbiota by NADCN. (A) Observed OTU richness of gut microbiota of healthy mice or colitis mice with different treatments. The α-diversity indexes of gut microbiota, including B) Shannon index and C) Chao1 index, among the different treatment groups. D) PCoA and E) NMDS analysis of the β-diversity in the gut microbiota of healthy mice or colitis mice with different treatments at the Amplicon Sequence Variant (ASV) level. Relative abundance of F) *Ruminococcaceae*, G) *Lactobacillaceae*, and H) *Enterobacteriaceae* in different treatment groups. (I) Relative abundance histogram of different species at the family level in different treatment groups. (J) Bubble plot of the relative abundance of top 25 bacterial genera in different treatment groups at the genus level. (K) Chord diagram showing the differentially abundant taxa among the groups at the family level. (L) Cladogram of the enriched taxa in the NADCN group or DSS-induced colitis group. Cladogram of the enriched taxa was performed at family, genus and species levels. The data are presented as the mean ± S.D., n = 4. Data are presented as mean ± S. D. p values were calculated via one-way ANOVA test. *$p < 0.05$.

group is greatly lower than other treatment groups (Fig. 7E), further confirming the robust and comprehensive anti-inflammatory effect of NADCN. Interestingly, the colonic tissues in the NADCN group possess more regulatory T cells (Treg; $CD4^+Foxp3^+$) than those in other treatment groups, reflecting the restored hemostasis of immune response (Figure S15). Consistently, as revealed by the RT-qPCR and western blot (WB) results, significantly reduced levels of *TNF-α*, *IL-1β*, and p-p65 are observed in the NADCN group than other treatment groups (Fig. 7F-H). Moreover, as shown in Figure S16, the quantitative results of the enzyme-linked immunosorbent assay (ELISA) assay further validating the synergistic anti-inflammatory performance of NADCN. Taken together, these results demonstrate that the NADCN possesses excellent anti-inflammatory efficacy against DSS-induced colitis through the synergistic effect of nanozyme-enabled redox regulation and OTUD1-meidated disruption of NF-κB signaling pathway (Fig. 7I).

Modulation of the gut microbiota by NADCN

Accumulating evidences from preclinical and clinical studies have consistently supported that dysbiosis of the gut microbiome plays a crucial role in the progression of IBD. Therefore, the gut microbiota changes of colitis mice after various therapies are examined by the 16S rDNA sequencing assay. As shown in Fig. 8A, the observed operational taxonomic unit (OTU) richness of the gut microbiota in the NADCN group is notably higher than that in the DSS-induced colitis group. Besides, the Shannon and Chao1 indices reveal a significant loss of bacterial community diversity in the DSS-induced colitis group, while the NADCN treatment could effectively restore the diversity of bacterial community to the level of healthy mice (Fig. 8B, C). Subsequently, β-diversity of gut microbiota composition among different groups is evaluated by the principal coordinate analysis (PCoA) and nonmetric multidimensional scaling (NDMS). Distinct from that of the IBD mice, the PCoA and NMDS plots indicate that the gut microbiota in the NADCN group partially overlaps with that in the healthy group (Fig. 8D, E), suggesting that NADCN treatment could effectively restore the disrupted gut microbiota composition in colitis mice. Moreover, compared to the DSS-induced colitis group, NADCN treatment significantly upregulates the abundance of beneficial microbiome, such as *Ruminococcaceae* and *Lactobacillaceae* (Fig. 8F, G), known to generate secondary bile acid and anti-inflammatory short-chain fatty acids (SCFA) [44–46]. Meanwhile, the NADCN treatment group exhibits a remarkably lower level of IBD-associated harmful bacteria *Enterobacteriaceae* than the DSS-induced colitis group (Fig. 8H, I), suggesting the good potential of NADCN to restore a healthy gut microbiota. Similar results are also visualized by the bubble chart, chord diagram, and cladogram from the linear discriminant analysis effect size (LEfSe) analysis (Fig. 8J-L), which exhibit differentially abundant bacterial taxa between the NADCN treatment group and DSS-induced colitis group. Specifically, the well-known pathogenic microbiome, such as *Enterobacteriaceae* and *Escherichia-Shigella* are enriched in colitis group, which decreases significantly in the NADCN group (Fig. 8J-L). Interestingly, the level of a well-known mucin-degrading gut microbiota, *Akkermansia muciniphila*, recovers to normal after the NADCN treatment, thus avoiding the excessive degradation of the colonic mucus barrier (Fig. 8J). Moreover, relative abundance of the beneficial bacteria, such as *Muribaculaceae*, *Lactobacillus*, *Lachnospiraceae*, *Lactobacillaceae*, and *Ruminococcaceae* is recovered after NADCN treatment, suggesting the crucial role of NADCN on restoring the healthy gut microbiota (Fig. 8J-L). In contrast, relative abundance of the beneficial bacteria, such as *Muribaculaceae*, *Lactobacillus*, *Lachnospiraceae*, *Lactobacillaceae*, and *Ruminococcaceae* is recovered after NADCN treatment, suggesting the crucial role of NADCN on restoring the healthy gut microbiota (Fig. 8J-L).

Motivated by the excellent efficacy of NADCN, the biosafety of NADCN were next evaluated. As shown in Figure S17A-C, NADCN exhibits excellent cellular biocompatibility in terms of cell viability (RAW264.7 cells and MODE-K epithelial cells) and hemolysis assay. Having confirmed that NADCN are not cellular toxic, we next evaluate the impact of NADCN on major organs and the blood system at animal level. H&E staining reveals that structures of major organs, such as colon, heart, liver, spleen, lung, and kidney, are not affected by the NADCN treatment, indicating the desirable biosafety and minimal side effects (Figure S17D). Meanwhile, the impact of NADCN treatment on the liver and kidney functions are evaluated by alanine aminotransferase (ALT), aspartate aminotransferase (AST), blood urea nitrogen (BUN), creatinine (CR), and uric acid (UA) assays. As shown in Figure S17E-I, the NADCN treatments have a limited impact on the liver and kidney function, indicating the significant potential and feasibility for clinical translation.

Conclusion

In summary, with the aim of designing DUB-based upstream anti-inflammatory therapies for IBD, this work proposes a nanozyme-enabled self-protection strategy to mitigate the activity loss of OTUD1 in the hostile oxidative inflammatory microenvironment. The encapsulated Pt nanozyme with SOD/CAT-mimetic activities could effectively eliminate the excessive ROS in the inflammatory microenvironment, thus preventing ROS from attacking the vulnerable cysteine (-SH) catalytic active center of co-delivered OTUD1. Moreover, compared to the downstream anti-inflammatory inhibitors, the inherent ability of OTUD1 to target the upstream of NF-κB pathway confers additional benefit. Indeed, benefiting from the synergistic effect of redox-active protection and upstream inhibition of NF-κB pathway, in vivo and in vitro studies demonstrate a remarkable anti-inflammatory performance for IBD treatment. To the best of our knowledge, this is the first strategy in which the artificial nanozyme is integrated to protect the vulnerable cysteine active-site of natural DUB, thus greatly advancing the biomedical application of fragile DUB. Beyond the specific design proposed here, this work is expected to afford a novel paradigm for designing highly efficient deubiquitylation therapy towards inflammatory diseases. The diverse integrations of ROS-scavenging nanozymes (Ceria nanozyme, Carbon dot nanozyme, etc.), cysteine DUBs (Cezanne, A20, etc.), and nanocarriers (Hydrogen-bonded organic frameworks (HOFs), Covalent organic frameworks (COFs) etc.) endow this nanozyme-augmented strategy with desirable universality and versatility, which will facilitate the development of anti-inflammatory therapies based on DUBs.

Materials and methods

Materials

Polyvinylpyrrolidone (PVP, Mw: 58,000 Da), chloroplatinic acid hydrate (H_2PtCl_6•6 H_2O), zinc nitrate hydrate ($Zn(NO_3)_2$·6 H_2O), fluorescein isothiocyanate (FITC), 2,2′-azino-bis (3-ethylbenzothiazoline-6-sulfonic acid) (ABTS), 8-anilino-1-naphthalenesulfonic acid (ANS) and tris (4,7-diphenyl-1,10-phenanthroline) ruthenium (II) dichloride complex ($[Ru(dpp)_3]Cl_2$) were obtained from Aladdin Reagent (Shanghai, China). 2-methylimidazole was purchased from Macklin Biochemical Co., Ltd (Shanghai, China). $NaBH_4$ was obtained from Tianjin Kemiou Chemical Reagent Co., Ltd (Tianjin, China). The natural DUB enzyme OTUD1 was obtained from Prof. Lingfeng Chen. Hydrogen peroxide (H_2O_2, 30 wt%) was bought from Sinopharm Chemical Reagent Co., Ltd (Beijing, China). Ubiquitin-7-amino-4-methylcoumarin (Ub-AMC) was bought from ABclonal Technology, Inc. (BSN, USA). Mitochondrial Superoxide Detection (MitoSox), SOD Assay Kit were obtained from DOJINDO Laboratories (Tokyo, Japan). 5,5′,6,6′-tetrachloro-1,1′,3,3′-tetraethylimidacarbocyanine iodide (JC-1) Mitochondrial Membrane Potential Assay Kit and Lyso-Tracker Red were bought from Yeasen Biotechnology Co., Ltd (Shanghai, China). RPMI 1640 medium and DMEM medium were obtained from Bio-Channel Biotechnology Co., Ltd (Nanjing, China). Fetal bovine serum (FBS) was bought from

Invigentech (CA, USA). DAPI, Actin-Tracker Red, BCA protein assay kit, CAT assay kit and ROS assay kit 2′-7′-dichlorofluorescin diacetate (DCFH-DA) were purchased from Beyotime Institute of Biotechnology (Shanghai, China). Cell Titer 96 AQueous One Solution Cell Proliferation Assay Kit was bought from Promega Biotech Co., Ltd (Beijing, China). Dextran Sulfate Sodium Salt (DSS, Mw: 36,000–50,000 Da) was purchased from MP Biomedicals (CA, USA). Protein Carbonyl assay kit, Myeloperoxidase (MPO) assay kit and Malondialdehyde (MDA) assay kit were purchased from Nanjing Jiancheng Bioengineering Institute (Nanjing, China). Wheat germ agglutinin (WGA) was obtained from AAT Bioquest, Inc. (CA, USA). GAPDH antibody (ET1601–4) and HRP Conjugated Goat anti-Rabbit IgG antibody (HA1001) were purchased from HuaAn Biotechnology Co., Ltd (Hangzhou, China). ZO-1 antibody (AF5145), Occludin-1 antibody (DF7504), Claudin-1 antibody (DF6919), HIF-1α antibody (AF1009), p65 antibody (AF5006), phosphorylated p65 (p-p65) antibody (AF2006), TNF-α antibody (AF7014), iNOS antibody (AF0199), and CD163 antibody (DF8235) were purchased from Affinity Biosciences Co., Ltd (Jiangsu, China). 8-OHdG antibody (bs-1278R), 4-hydroxynonenal (4-HNE) antibody (bs-6313R), and Foxp3 antibody (bs-10211R) were purchased from Biosynthesis Biotechnology Co., Ltd (Beijing, China), CD4 antibody (100505) was purchased from BioLegend, Inc. (CA, USA). Lipopolysaccharides (LPS) and FITC-dextran 4 kDa (FD-4) were purchased from Sigma-Aldrich (MO, USA). Primers were bought from Generay Biotech Co., Ltd (Shanghai, China). AG RNAex Pro Reagent (AG21101), Evo M-MLV RT Mix kit (AG11734) and SYBR@ Green Premix Pro Taq HS qPCR kit (AG11733) were Accurate Biotechnology Co. LTD (Changsha, China). Ferrous chloride tetrahydrate ($FeCl_2$•4 H_2O) was acquired from Xiya Reagent (Shandong, China). Alexa-488-maleimide were purchased from AAT Bioquest (CA, USA). Mouse TNF-α ELISA Kit (EK0527), Mouse IL-6 ELISA Kit (EK0411), and Mouse IL-1β ELISA Kit (EK0394) were purchased from Boster Biological technology (Wuhan, China).

Characterization

TEM and STEM-EDX element distribution images were taken by FEI Tecnai F20 (FEI, USA). DLS was characterized using a Zetasizer Nano ZS90 (Malvern Instruments, UK). XRD patterns were recorded with Bruker D8-Advanced X-pert Powder X-ray diffractometer (Bruker, Germany). XPS spectra were collected with K-Alpha X-ray photoelectron spectrometer (ThermoFisher Scientific, USA). The UV–vis absorption spectra of samples were obtained using a UV-2600 spectrophotometer (Shimadzu, Japan). Raman mapping was recorded in a WITec alpha 300RA confocal Raman microscope (WITec, Germany). Circular dichroism (CD) spectra were recorded on a Chirascan V100 spectropolarimeter (Applied Photophysics, England). The fluorescence spectrum was determined using F-4600 fluorescence spectrometer (HITACHI, Japan). The fluorescence intensity was collected in a Synergy H1 microplate fluorescence reader device (BioTek, USA). The fluorescence images were collected by an Eclipse Ti2 confocal laser scanning fluorescence microscope (CLSM) (Nikon, Japan). In vivo biodistribution was detected using a small animal imaging system (Caliper, USA). PA intensity and PA images were collected by inVision 256 preclinical photoacoustic computerized tomography scanner (iThera Medical, Germany). Protein bands were captured by using Invitrogen iBright 1500 Imaging System (ThermoFisher Scientific, USA). RT-qPCRs were tested by using CFX96 Real Time System C1000 Touch Thermal Cycler (BioRad, USA). Endoscopic images of the mice were obtained using a MiniScope 2 V multifunctional small animal soft endoscope (SHINOVA, China). The freeze-dried NADCN was prepared by FreeZone Plus 6 L vertical freedrying system (Labconco, USA).

Preparation of PtNZ

PtNZ was prepared according to the previous reports [47]. Briefly, 5 mL polyvinylpyrrolidone (PVP, 2.2 wt%) solution was added into 5 mL of chloroplatinic acid hydrate (H_2PtCl_6•6 H_2O, 0.05 wt%) solution. After stirring for 20 min, 200 μL freshly prepared sodium borohydride ($NaBH_4$, 100 mM) solution was slowly dropped into above medium and constantly stirred for 12 h, then the as-prepared PtNZ was collected by acetone precipitation. Subsequently, the product was washed for three times to remove excessive free PVP and finally dissolved in deionized water for further use.

Protein expression and purification

Bacterial expression constructs of OTUD1 were engineered by cloning the OTUD1 gene encoding OUT domain into pET30. Transformed *Escherichia coli* cells were grown in LB medium at 37 °C until the OD_{600} reached approximately 0.8, 0.5 mM IPTG was added and induced for another 14–18 h at 18 °C. Cells were harvested by centrifugation at 5000 rpm for 8 min, and the cells were resuspended in 40 mL lysis buffer (50 mM Tris, 500 mM NaCl, pH 7.5, protease inhibitor) and lysed using a homogenizer. The lysate was centrifuged at 12000 rpm for 25 min at 4 °C, and the supernatant was collected. The supernatant was passed through a Ni-NTA affinity chromatography. The natural DUB enzyme OTUD1 was eluted with elution buffer containing 300 mM imidazole. The eluted protein was further purified by gel filtration chromatography in HEPES buffer through the Superdex 200 column to collect the natural DUB enzyme OTUD1.

Synthes is of NADCN

50 μL OTUD1 solution and 50 μL PtNZ solution at different feed ratios were incubated with 900 μL 2-methylimidazole (2-MIM, 3.5 M) aqueous solution for 20 min. Under stirring, 100 μL zinc nitrate hydrate ($Zn(NO_3)_2$·6 H_2O, 0.5 M) aqueous solution was dropped into above reaction system. Finally, the mixture was kept at 4 °C for 12 h. The obtained product was washed for three times with water by centrifugation (11000 rpm, 30 min). For comparison, ACN and NCN were prepared with the similar procedure of NADCN without adding OTUD1 and PtNZ, respectively. In addition, to evaluate whether freeze-drying would impact the activity of OTUD1, we freeze-dried freshly prepared NADCN and stored obtained powder at −20 °C for further use. Specifically, the freshly prepared NADCN was frozen overnight at −80 °C and freeze-dried the day after in a freeze-drier (LABCONCO, 6-PLUS) for 24 h.

To gain the cellular uptake behaviors and mucus adhesion properties of NADCN, FITC-tagged OTUD1 and FITC-tagged NADCN were synthesized. Briefly, 10 mL of $NaHCO_3$ solution (0.1 M) containing 40 mg OTUD1 was mixed with 1 mL of DMSO containing 4 mg FITC and incubated overnight in dark [48]. The as-prepared FITC-tagged OTUD1 was used to synthesize FITC-tagged NADCN by using the same method as NADCN. Then the product was collected by centrifugation (11000 rpm, 30 min) and washed for three times with water to remove excessive dye and reactants. To determine the biodistribution of NADCN in vivo, ICG-loaded NADCN was prepared by using the similar procedure of NADCN due to its advantages of deep tissue penetration and low tissue auto-fluorescence. In brief, 50 μL OTUD1 solution (50 μg/mL), 50 μL PtNZ solution and 50 μL ICG solution (4 mg/mL) were incubated with 900 μL 2-MIM (3.5 M) aqueous solution for 20 min followed by the addition of 100 μL $Zn(NO_3)_2$·6 H_2O (0.5 M) aqueous solution. The mixture was then kept at 4 °C for 12 h. After centrifugation and washing for three times, the obtained FITC-tagged NADCN and ICG-loaded NADCN was redispersed in deionized water and stored in dark for further use.

Evaluation of enzyme-mimic activities of PtNZ

The SOD-mimetic activity of PtNZ solution with different concentrations (0.125, 0.25, 0.5, 1 mg/mL) was measured using a SOD Assay Kit WST. The SOD-mimetic activity expressed as the percentage inhibition of WST reaction with superoxide was calculated according to the

manufacturer's instructions. CAT-mimetic activity of PtNZ solution with different concentrations (0.125, 0.25, 0.5, 1 mg/mL) was performed using a CAT Assay Kit. All the assays were carried out following the commercially available standard protocols. Subsequently, the CAT-mimetic O_2 production of PtNZ was further measured. Briefly, 5 mL H_2O_2 (0.01 M) and 1 mL PtNZ solution with different concentrations (0.125, 0.25, 0.5, 1 mg/mL) were mixed at room temperature, and the dissolved oxygen levels were real-time recorded by Dissolved Oxygen Meter.

Stability of NADCN in Different Physiological Solutions

To evaluate the stability of NADCN in different physiological solutions, NADCN was centrifuged at 11000 rpm for 30 min and then resuspended in deionized (DI) water, PBS and simulated colon fluids (SCF). The dynamic light scattering (DLS) data of NADCN were measured at 0 h, 6 h, 12 h, 24 h, 48 h, and 72 h using a Zetasizer Nano ZS90 (Malvern Instruments, UK).

Evaluation of the structural degradation performance of NADCN under acidic condition

To evaluate the structural degradation performance of NADCN, NADCN was suspended in neutral (pH 7.4) and acidic PBS buffers (pH 5.5). After incubation for 24 h, the morphology and dimensions of the samples treated with different pH values were observed using TEM.

Evaluation of the total antioxidant capacity of NADCN

To evaluate the ROS scavenging capacity of NADCN, $ABTS^{+\cdot}$ elimination assay was applied. Briefly, the $ABTS^{+\cdot}$ radical solution was obtained by incubating ABTS (1.4 mM) with $K_2S_2O_8$ (0.49 mM) in dark overnight. Then, different concentrations of NADCN (0, 1, 2, 4, 8 mg/mL) were incubated with $ABTS^{+\cdot}$ radical solution for 1 h, respectively. Afterward, the UV–vis spectra were recorded using a UV-2600 spectrophotometer and the time-course $ABTS^{+\cdot}$ scavenging efficiency was calculated by determining the UV–vis absorbance at 734 nm. The formula used to calculate $ABTS^{+\cdot}$ scavenging rate was: $ABTS^{+\cdot}$ scavenging rate (%) $= (1 - A_{sample}/A_{control}) \times 100$ %, where $A_{control}$ is the absorbance of the $ABTS^{+\cdot}$ radical solution without any antioxidant, and A_{sample} is the absorbance of the $ABTS^{+\cdot}$ radical solution after the reaction with different concentrations of NADCN, respectively.

Oxidative resistance and self-protective capacity of NADCN

To assess the ROS damage resistance and self-protective capacity of NADCN, Raman measurements, CD spectroscopy, intrinsic fluorescence spectroscopy, ANS fluorescence spectroscopy and Ub-AMC assay were carried out. NCN and NADCN with 50 μg/mL of OTUD1 were incubated with PBS, H_2O_2 (200 μM) or •OH (200 μM) at 37 ℃ for 30 min. 600 μL of $FeCl_2$•4 H_2O (5 mM) mixed with 400 μL of H_2O_2 (5 mM) was prepared as •OH working solution based on the Fenton reaction. First, Raman measurements were carried out in a WITec alpha 300RA confocal Raman microscope with a 532 nm laser. Then, 200 μL samples were loaded into a quartz cuvette of 1 mm path length and the CD spectra were measured by Chirascan V100 spectropolarimeter at room temperature. Next, the intrinsic fluorescence of the PBS or H_2O_2-treated NCN and NADCN samples were recorded by using a fluorescence spectrometer. The excitation wavelength was 280 nm and the emission spectra were recorded from 300 to 420 nm. Subsequently, the PBS, H_2O_2 or •OH-treated NCN and NADCN samples were incubated with ANS (50 mM) for 1 min. Changes in the ANS fluorescence intensity were determined with the excitation wavelength at 380 nm and the emission wavelength from 400 to 600 nm using a fluorescence spectrometer. Finally, the Ub-AMC assay was carried out in a Synergy H1 microplate fluorescence reader device. NCN and NADCN with 1.5 mg/mL of OTUD1 were incubated with PBS or H_2O_2 (200 μM) at 37 ℃ for 30 min. The PBS or H_2O_2-treated NCN and NADCN samples were collected by centrifugation and redispersed in 150 μL Tris-HCl (50 mM, pH = 8.5) solution. After being incubated for 15 min at 30 ℃, 9.75 μL Ub-AMC (5 μM) was added and AMC fluorescence was detected with an excitation at 380 nm and emission at 470 nm. Moreover, we employed the thiol-reactive fluorophore ALM-488 to precisely quantify the -SH content after various treatments. First, NCN and NADCN with 50 μg/mL of OTUD1 were incubated with PBS, H_2O_2 (200 μM) or •OH (200 μM) at 37℃ for 30 min. Then ALM-488 (1 mM) was added to each group and incubated for an additional 30 min. Subsequently, the mixtures were centrifuged at 14000 rpm for 30 min to remove excessive free probe and then resuspended in PBS. Fluorescence images and intensities of each group were recorded using a small animal imaging system (Caliper, USA). The fluorescence intensity of ALM-488 ($\lambda ex = 499$ nm, $\lambda em = 520$ nm) in each group was measured by Synergy H1 microplate fluorescence reader.

Cell culture

MODE-K cells were cultured in RPMI 1640 medium containing 10 % fetal bovine serum and 1 % penicillin/streptomycin. RAW 264.7 macrophage cells were cultured in high glucose DMEM medium containing 10 % fetal bovine serum. All cells were obtained via commercial approaches. In a normal condition, cells were cultured at 37 °C in a 5 % CO_2 and 95 % air atmosphere (about 20 % O_2). In hypoxia related experiments, RAW 264.7 macrophage cells were cultured in a hypoxia incubator chamber filled with hypoxic atmosphere (1 % O_2, 5 % CO_2, and 94 % N_2) at 37 ℃.

Biocompatibility tests in vitro

RAW264.7 macrophage cells were seeded into 96-well plates overnight. Then, ACN, NCN and NADCN with different concentrations (0, 10, 20, 30, 40, 50 μg/mL) were added and incubated with cells. After cultured for 24 h, the viability of RAW264.7 macrophage cells was evaluated by using a Cell Titer 96 AQueous One Solution Cell Proliferation Assay Kit. Subsequently, the hemocompatibility of NADCN was evaluated by incubating freshly collected red blood cells (RBCs) with Triton X-100, saline solution, ACN (50 μg/mL), NCN (50 μg/mL) and NADCN (50 μg/mL) at 37 ℃ for 1 h. After the incubation, the RBCs were centrifuged with 3000 rpm for 15 min to collect the supernatant. The supernatant was transferred into 96-well plate and the OD value at 540 nm was detected. Finally, the 96-well plate was photographed. Hemolysis (%) $= (A_{sample} - A_{negative})/(A_{positive} - A_{negative}) \times 100$ %, where $A_{negative}$ is the OD value of the supplement of saline solution treated-RBCs, and $A_{positive}$ is the OD value of the supplement of Triton X-100 treated-RBCs.

ROS scavenging in vitro

RAW264.7 macrophage cells were seeded in confocal dishes and cultured overnight to achieve an appropriate cell density. Then, the cells were cultured with medium containing PBS, ACN (50 μg/mL), NCN (50 μg/mL) and NADCN (50 μg/mL) along with LPS (500 ng/mL) under hypoxic condition (1 % O_2) for 3 h. After washing with PBS for three times, serum-free medium containing DCFH-DA probe (10 μM) was added to every dish and incubated at 37 ℃ for 30 min. After washing for three times with PBS, the cells were fixed with 4 % paraformaldehyde for 10 min and DAPI was used to stained for cells for 10 min. Finally, the fluorescence images were acquired by CLSM and quantified using Image J software.

Mitochondrial function assessment in vitro

RAW264.7 macrophage cells were seeded in confocal dishes and

cultured overnight to achieve an appropriate cell density. Then, the cells were cultured with medium containing PBS, ACN (50 μg/mL), NCN (50 μg/mL) and NADCN (50 μg/mL) along with LPS (500 ng/mL) under hypoxic condition (1 % O_2) for 3 h. After washing with PBS for three times, serum-free medium containing MitoSox working solution (10 μM) was added into each dish and incubated for 30 min at 37 ℃ to determine mitochondrial superoxide generation in cells. Afterward, cells were fixed with 4 % paraformaldehyde for 10 min and rinsed with PBS before DAPI staining. To assess the changes of mitochondrial membrane potential (MMP) in cells, JC-1 working solution was added into confocal dishes and incubated for 20 min at 37 ℃ before washing dishes with PBS for three times. Finally, cells were visualized by using CLSM and quantified using Image J software.

Intracellular O_2 levels detection in vitro

RAW264.7 macrophage cells were seeded in confocal dishes and cultured overnight to achieve an appropriate cell density. Then, the cells were cultured with medium containing PBS, ACN (50 μg/mL), NCN (50 μg/mL) and NADCN (50 μg/mL) along with LPS (500 ng/mL) under hypoxic condition (1 % O_2) for 3 h, followed with washing for three times with PBS. Afterward, the medium in each dish was replaced with serum-free medium containing O_2 indicator $[Ru(dpp)_3]Cl_2$ (50 μg/mL) for 30 min at 37 ℃. After washing for several times, the cells were fixed with 4 % paraformaldehyde for 10 min. Afterward, the cells were rinsed with PBS and incubated with DAPI staining solution for another 10 min. Finally, the intracellular fluorescence of $[Ru(dpp)_3]Cl_2$ ($\lambda_{ex} = 450$, $\lambda_{em} = 600$ nm) was detected by CLSM and quantified using Image J software.

Cell immunofluorescence staining assay

RAW264.7 macrophage cells were seeded in confocal dishes and cultured overnight to achieve an appropriate cell density. Then, the cells were cultured with medium containing PBS, ACN (50 μg/mL), NCN (50 μg/mL), fresh prepared NADCN (50 μg/mL) at varying Pt/OTUD1 feed ratios (0:1, 2.5:1, 5:1, 10:1, and 20:1) and freeze dried NADCN (50 μg/mL) along with LPS (500 ng/mL) under hypoxic condition (1 % O_2) for 3 h, followed with washing for three times with PBS. Next, cells were fixed with 10 % neutral formalin at room temperature for 15 min. After washing thrice with PBS, cells were permeabilized with 0.3 % Triton X-100 at room temperature for another 15 min followed by washing with cold PBS. 10 % BSA was added and sealed at room temperature for 30 min to block nonspecific antibody binding, and cells were incubated with diluted primary antibody including HIF-1α, TNF-α and p-p65 overnight at 4 °C. After a thorough washing with cold PBS, cells were incubated with diluted secondary antibody at room temperature for 1 h, followed by washing with PBS twice. Finally, cells were stained with Actin-Tracker Red for 30 min followed with DAPI staining and washed for three times. Immunofluorescence images of the cells were acquired by CLSM.

Real-time qPCR analysis

RAW264.7 macrophage cells were seeded in 12-well plates and incubated overnight. Then, the cells were cultured with medium containing PBS, ACN (50 μg/mL), NCN (50 μg/mL) and NADCN (50 μg/mL) along with LPS (500 ng/mL) under hypoxic condition (1 % O_2) for 3 h. After washing for three times with cold PBS, the normoxic and hypoxia-treated cells were harvested and the total ribonucleic acid (RNA) was extracted using Trizol according to the manufacturer's instruction. After analyzing the concentration and quality of RNA using Nanodrop, 1 μg of RNA samples were transcribed into complementary deoxyribonucleic acid (cDNA) using Evo M-MLV RT Mix kit. RT-qPCR was performed using a CFX96 Real Time System C1000 Touch Thermal Cycler. The relative expression levels of target genes including *TNF-α*, *IL-1β*, *IL-6* were then normalized with GAPDH, and analyzed using the $2^{-\Delta\Delta CT}$ method. The sequences of primers are listed as Table 1:

Western blotting

RAW264.7 macrophage cells were seeded in 12-well plates and incubated overnight. Then, the cells were cultured with medium containing PBS, ACN (50 μg/mL), NCN (50 μg/mL) and NADCN (50 μg/mL) along with LPS (500 ng/mL) or blank medium under hypoxic condition (1 % O_2) for 3 h. After washing for three times with cold PBS, proteins from cells in each group were lysed in RIPA buffer containing protease and phosphatase inhibitors. Next, the total amount of protein in each sample was determined using a BCA protein assay kit. Then, equal amount of protein in each group was separated via sodium dodecyl sulfate-polyacrylamide (SDS-PAGE) gel electrophoresis and transferred to poly (vinylidene fluoride) fluoride (PVDF) membranes. After being blocked in 5 % BSA at room temperature for 1 h and washed for three times with TBST, the membranes were incubated with primary antibodies targeting TNF-α, p65, p-p65 and GAPDH at 4 ℃ overnight. After washing thrice with TBST, the membranes were incubated with the secondary antibody for 2 h at room temperature. After washing thrice with TBST, the proteins in the membranes were visualized using an Enhanced Chemiluminescence (ECL) kit. Finally, the blots were imaged by using Invitrogen iBright 1500 Imaging System.

Enzyme-linked immunoadsorbent assay (ELISA) analysis

RAW264.7 macrophage cells were seeded in 12-well plates and incubated overnight. Then, the cells were cultured with medium containing PBS, freshly prepared NADCN (50 μg/mL) at varying Pt/OTUD1 feed ratios (0:1, 2.5:1, 5:1, 10:1, and 20:1) and freeze-dried NADCN (50 μg/mL) along with LPS (500 ng/mL) under hypoxic conditions (1 % O_2) for 3 h. The cell supernatants were collected from each group, and the levels of TNF-α in the supernatants were measured using ELISA. The specific implementation steps can be found in the user manual of the relevant kit.

Construction of DSS-induced IBD mice model and treatments

C57BL/6 mice (male, 8 weeks, 20–23 g) were purchased from Experimental Animal Center of Hangzhou Medical College (Hangzhou, China). All the mice were acclimatized for seven days before inclusion in the experiment. Then, all the mice were randomly divided into five groups: healthy mice without any treatment (Healthy), IBD mice treated with PBS (IBD), IBD mice treated with ACN (ACN), IBD mice treated with NCN (NCN) and IBD mice treated with NADCN (NADCN). The mice from each group received rectal administration of PBS, ACN (10 mg/kg), NCN (10 mg/kg) and NADCN (10 mg/kg) on days 1, 3, 5 and 7. All the mice were euthanized after endoscopy on the 8th day. During the experiment, body weight change, consistency of stool and fecal blood were monitored daily to determine the DAI of each mouse. On the 8th day, endoscopic images of the mice from each group were obtained to determine the intestinal conditions using a multifunctional small animal soft endoscope. Subsequently, all the mice were euthanized, the length of colon and the weight of spleen from each mouse were measured. In addition, colonic tissues were collected and divided into several sections for further analysis including histological analysis, immunofluorescence staining, western blotting, RT-qPCR, ELISA assay, MPO assay, MDA

Table 1
List of primers.

Gene	Forward primer	Reverse primer
TNF-α	GGTGCCTATGTCTCAGCCTCTT	GCCATAGAACTGATGAGAGGGAG
IL−6	TACCACTTCACAAGTCGGAGGC	CTGCAAGTGCATCATCGTTGTTC
IL−1β	TGGACCTTCCAGGATGAGGACA	GTTCATCTCGGAGCCTGTAGTG
GAPDH	CATCACTGCCACCCAGAAGACTG	ATGCCAGTGAGCTTCCCGTTCAG

assay and protein carbonyl assay. All animal experiments have been approved by the Experimental Animal Ethical Committee of Hangzhou Medical College (ZJCLA-IACUC-20010155).

Histological and immunofluorescence staining of colonic tissues

The dissected colonic tissues from each group were fixed in 4 % paraformaldehyde and embedded in paraffin followed cut into 5 μm tissue slices for H&E staining, AB-PAS staining and immunofluorescence staining (ZO-1, Claudin-1, Occludin-1, 8-OHdG, 4-HNE, HIF-1α, TNF-α, CD163, iNOS, CD4 and Foxp3). The histopathology score was measured via H&E staining according to previous reports [49].

IVIS imaging in vivo

To determine the biodistribution of NADCN in colon, IBD mice were intra-rectally given NADCN (10 mg/kg, 200 μL) after 5 days of DSS induction. For comparison, healthy mice were also intra-rectally given NADCN (10 mg/kg, 200 μL). After 6 h, all the mice were euthanized and colons were extracted for IVIS imaging. Fluorescence images and intensities were recorded by small animal imaging system for further use.

Mucus adhesion properties of NADCN

Healthy mice and IBD mice were intra-rectally given FITC-tagged NADCN (10 mg/kg, 200 μL) after 5 days of DSS induction. After 6 h, mice were euthanized and the colon tissues were excised for cryostat section. After WGA staining for mucosal, the 3D images of the mucosal and NADCN adhered were obtained by CLSM. To further evaluate the interaction between macrophages and NADCN, immunofluorescence staining (CD68 and DAPI) of treated colon from healthy or IBD mice were carried out and visualized by CLSM.

PAI capacity of NADCN

PA intensities and PA images were conducted by inVision 256 preclinical photoacoustic computerized tomography scanner. First, PA signal intensities and images of NADCN at different concentrations (0, 12.5, 25, 50, 100, 200 μg/mL) were scanned using the wavelength at 800 nm by inVision 256 preclinical photoacoustic computerized tomography scanner. To measure the oxygen microbubbles-enabled PA imaging of NADCN, different concentrations of H_2O_2 aqueous solution (0, 100, 200, 400, 600, 800, 1000 μM) were added into NADCN (12.5 μg/mL) solution. After 5 min, PA intensities and PA images were recorded. Subsequently, IBD mice were intra-rectally given NADCN (10 mg/kg, 200 μL) after 5 days of DSS induction. For comparison, healthy mice were also intra-rectally given NADCN (10 mg/kg, 200 μL). After 6 h, the mice were anesthetized with 5 % isoflurane mixed with air and scanned using the wavelength at 800 nm. Cross-section PA images of the treated colon from healthy or IBD mice were collected and quantified then.

Intestinal permeability test

After 7 days of DSS induction, all the mice were fasted for 4 h followed by oral given FD-4 solution (500 mg/kg). After 4 h treatment, blood of each mouse was collected and centrifuged (1000 rpm) for 15 min to acquire serum. The fluorescence intensity of FD-4 in serum (λ_{ex} = 485 nm, λ_{em} = 520 nm) was determined using a Synergy H1 microplate fluorescence reader device.

Biosafety evaluation in vivo

Healthy C57 BL/6 mice were randomly divided into two groups: The control group treated with 200 μL PBS every other day for four times in total and the NADCN group treated with 200 μL NADCN (10 mg/kg) every other day for four times in total. The mice were euthanized 28 days after treatment. To evaluate the biosafety in vivo, the major organs including heart, liver, spleen, lung, kidney and colon were harvested for H&E staining to analyzed the histological changes. The serum of each mouse was also collected to analyze the levels of alanine aminotransferase (ALT), aspartate aminotransferase (AST), blood urea nitrogen (BUN), blood creatinine (CR) and uric acid (UA), which indicated the function of liver and kidney.

16S rDNA sequencing and analysis

The feces from each group of mice euthanized on the 8th day were collected for 16S rDNA sequencing and analysis. The sequencing and analysis of 16S rDNA was performed at LC-Bio Technology Co., Ltd, Hang Zhou, Zhejiang Province, China. DNA from different groups of colon samples was extracted using the E.Z.N.A. ®Stool DNA Kit (D4015, Omega, Inc., USA) according to manufacturer's instructions, followed by PCR amplification, purifying the PCR products by AMPure XT beads (Beckman Coulter Genomics, Danvers, MA, USA), quantifying the products by Qubit (Invitrogen, USA) and assessment of amplicon library. The libraries were sequenced on NovaSeq PE250 platform according to the manufacturer's recommendations. Alpha diversity and Beta diversity were calculated by QIIME2.

Statistical analysis

Statistical analysis was performed by Origin 2021. The Mannu-Whitney U-test and one-way analysis of variance were used for calculating the statistical significances. $p < 0.05$ was considered of statistical significance. LEfSe analysis (LDA score threshold: 3.5) was used for quantitative analysis of biomarkers within different groups for 16S rDNA analysis. Data were presented as mean ± standard deviation (S.D.) with sample size ($n \geq 3$).

Author statement

Haibin Wu conceiving and designed the study. Shuhan Shi and Lenan Xu performed the major experiments and prepared the figures and tables. Ziying Zheng, Ziyan Huang, Yi Qiu, Keyun Yang, YuTing Xie, Cheng Xu and Mincong Huang participated in the animal experiments. Tianyang Xu, Jixiang Zhang and Guohuan Zeng synthesized nanoparticles. Lingfeng Chen performed the protein expression and purification. Shuhan Shi, Haibin Wu and Lenan Xu analyzed and interpreted the data. Haibin Wu, Qian Chen and Shuhan Shi wrote and modified the paper. Guang Liang, Daishun Ling and Qian Chen supervised the study. Haibin Wu and Guang Liang were responsible for funding acquisition. Haibin Wu, Shuhan Shi and Lenan Xu contributed equally to this work. All authors provided valuable suggestions on the research and the paper.

CRediT authorship contribution statement

Liang Guang: Supervision, Resources, Funding acquisition. **Qiu Yi:** Validation, Investigation, Data curation. **Ling Daishun:** Supervision, Resources. **Huang Ziyan:** Validation, Investigation, Data curation. **Chen Qian:** Writing – review & editing, Writing – original draft. **Zheng Ziying:** Validation, Investigation, Data curation. **Huang Mincong:** Resources. **Xu Lenan:** Writing – original draft, Visualization, Validation, Methodology, Investigation, Formal analysis, Data curation. **Xu Cheng:** Validation, Investigation. **Xie Yuting:** Validation, Investigation. **Yang Keyun:** Validation, Investigation. **Zhang Jixiang:** Validation, Investigation. **Shi Shuhan:** Writing – review & editing, Writing – original draft, Visualization, Validation, Methodology, Investigation, Formal analysis, Data curation. **Chen Lingfeng:** Resources. **Wu Haibin:** Writing – review & editing, Writing – original draft, Visualization, Supervision, Resources, Project administration, Methodology, Investigation, Funding acquisition, Data curation, Conceptualization. **Zeng Guohuan:**

Validation, Investigation. **Xu Tianyang:** Validation, Investigation.

Declaration of Competing Interest

The authors declare that they have no known competing financial interests or personal relationships that could have appeared to influence the work reported in this paper.

Acknowledgments

We gratefully acknowledge the support from the National Natural Science Foundation of China (32201161 to H.W.), Zhejiang Provincial Key Scientific Project (2021C03041 to G.L.), Zhejiang Special Support Program for Young High-level Talents (to H.W.), Basic Scientific Research Funds of Department of Education of Zhejiang Province (KYZD202205 to H.W.), and Hangzhou Medical College Qiuzhen Talent Project (00004F1RCYJ2209 to H.W.).

Appendix A. Supporting information

Supplementary data associated with this article can be found in the online version at doi:10.1016/j.nantod.2025.102735.

Data availability

Data will be made available on request.

References

[1] V. Jairath, B.G. Feagan, Lancet Gastroenterol. Hepatol. 5 (2020) 2–3.
[2] T. Jin, H. Lu, Q. Zhou, D. Chen, Y. Zeng, J. Shi, Y. Zhang, X. Wang, X. Shen, X. Cai, Sci 11 (2024) 2308092.
[3] P. Zhao, X. Xia, X. Xu, K.K.C. Leung, A. Rai, Y. Deng, B. Yang, H. Lai, X. Peng, P. Shi, H. Zhang, P.W.Y. Chiu, L. Bian, Nat. Commun. 12 (2021) 7162.
[4] D. Zhong, K. Jin, R. Wang, B. Chen, J. Zhang, C. Ren, X. Chen, J. Lu, M. Zhou, Adv. Mater. 36 (2024) 2312275.
[5] B. Barberio, M. Zamani, C.J. Black, E.V. Savarino, A.C. Ford, Lancet Gastroenterol. Hepatol. 6 (2021) 359–370.
[6] S.C. Shah, S.H. Itzkowitz, Gastroenterology 162 (2022), 715-730.e713.
[7] M.F. Neurath, Nat. Rev. Immunol. (2024).
[8] S.A. Hendler, B.L. Cohen, J.-F. Colombel, B.E. Sands, L. Mayer, S. Agarwal, J. Crohns Colitis 9 (2015) 266–275.
[9] J. Moreau, E. Mas, Curr. Opin. Pharm. 25 (2015) 56–61.
[10] A. Bourchany, C. Gilletta De Saint-Joseph, A. Breton, F. Barreau, E. Mas, Curr. Opin. Pharm. 54 (2020) 51–58.
[11] T.E.T. Mevissen, D. Komander, Annu. Rev. Biochem 86 (2017) 159–192.
[12] J. Han, Z. Fang, B. Han, B. Ye, W. Lin, Y. Jiang, X. Han, X. Wang, G. Wu, Y. Wang, G. Liang, Nat. Cardiovasc Res 2 (2023) 764–777.
[13] J. Zheng, X. Li, F. Zhang, C. Li, X. Zhang, F. Wang, J. Qi, W. Cui, L. Deng, Adv. Healthc. Mater. 13 (2023) 2402117.
[14] I. Mitxitorena, D. Somma, J.P. Mitchell, M. Lepistö, C. Tyrchan, E.L. Smith, P. A. Kiely, H. Walden, K. Keeshan, R.J. Carmody, J. Biol. Chem. 295 (2020) 11754–11763.
[15] P. Palazón-Riquelme, J.D. Worboys, J. Green, A. Valera, F. Martín-Sánchez, C. Pellegrini, D. Brough, G. López-Castejón, EMBO Rep. 19 (2018) e44766.
[16] X.-M. Wang, C. Yang, Y. Zhao, Z.-G. Xu, W. Yang, P. Wang, D. Lin, B. Xiong, J.-Y. Fang, C. Dong, B. Zhong, Nat. Cancer 1 (2020) 811–825.
[17] B. Wu, L. Qiang, Y. Zhang, Y. Fu, M. Zhao, Z. Lei, Z. Lu, Y.-G. Wei, H. Dai, Y. Ge, M. Liu, X. Zhou, Z. Peng, H. Li, C.-P. Cui, J. Wang, H. Zheng, C.H. Liu, L. Zhang, Cell. Mol. Immunol. 19 (2022) 276–289.
[18] K. Enesa, M. Zakkar, H. Chaudhury, L.A. Luong, L. Rawlinson, J.C. Mason, D. O. Haskard, J.L.E. Dean, P.C. Evans, J. Biol. Chem. 283 (2008) 7036–7045.
[19] Tycho E.T. Mevissen, Manuela K. Hospenthal, Paul P. Geurink, Paul R. Elliott, M. Akutsu, N. Arnaudo, R. Ekkebus, Y. Kulathu, T. Wauer, F. El Oualid, Stefan M. V. Freund, H. Ovaa, D. Komander, Cell 154 (2013) 169–184.
[20] N.A. Snyder, G.M. Silva, J. Biol. Chem. 297 (2021).
[21] C. Pereira, D. Grácio, J.P. Teixeira, F. Magro, Inflamm. Bowel Dis. 21 (2015) 2403–2417.
[22] A.R. Bourgonje, M. Feelisch, K.N. Faber, A. Pasch, G. Dijkstra, H. van Goor, Trends Mol. Med. 26 (2020) 1034–1046.
[23] J. Sheng, Y. Wu, H. Ding, K. Feng, Y. Shen, Y. Zhang, N. Gu, Adv. Mater. 36 (2024) 2211210.
[24] Z. Deng, W. Ma, C. Ding, C. Wei, B. Gao, Y. Zhu, Y. Zhang, F. Wu, M. Zhang, R. Li, M. Zhang, Nano Today 53 (2023) 102044.
[25] A. Yuan, F. Xia, Q. Bian, H. Wu, Y. Gu, T. Wang, R. Wang, L. Huang, Q. Huang, Y. Rao, D. Ling, F. Li, J. Gao, ACS Nano 15 (2021) 13759–13769.
[26] S. Zhao, Y. Li, Q. Liu, S. Li, Y. Cheng, C. Cheng, Z. Sun, Y. Du, C.J. Butch, H. Wei, Adv. Funct. Mater. 30 (2020) 2004692.
[27] J. Mu, C. Li, Y. Shi, G. Liu, J. Zou, D.-Y. Zhang, C. Jiang, X. Wang, L. He, P. Huang, Y. Yin, X. Chen, Nat. Commun. 13 (2022) 2513.
[28] Z. Sun, Q. Liu, X. Wang, J. Wu, X. Hu, M. Liu, X. Zhang, Y. Wei, Z. Liu, H. Liu, R. Chen, F. Wang, A.C. Midgley, A. Li, X. Yan, Y. Wang, J. Zhuang, X. Huang, Theranostics 12 (2022) 1132–1147.
[29] H. Wu, F. Li, W. Shao, J. Gao, D. Ling, ACS Cent. Sci. 5 (2019) 477–485.
[30] W. Zhen, Y. Liu, L. Lin, J. Bai, X. Jia, H. Tian, X. Jiang, Angew. Chem., Int. Ed. 57 (2018) 10309–10313.
[31] B.P. Carpenter, B. Rose, E.M. Olivas, M.X. Navarro, A.R. Talosig, P.J. Hurst, G. Di Palma, L. Xing, R. Guha, S.M. Copp, J.P. Patterson, J. Mater. Chem. A 12 (2024) 813–823.
[32] A. Micsonai, F. Wien, L. Kernya, Y.-H. Lee, Y. Goto, M. Réfrégiers, J. Kardos, Proc. Natl. Acad. Sci. U. S. A. 112 (2015) E3095–E3103.
[33] S. Puri, S.-T.D. Hsu, J. Mol. Biol. 433 (2021) 166879.
[34] R.Q. Grove, S.J. Karpowicz, Free Radic. Biol. Med. 108 (2017) 575–584.
[35] K. Bartels, A. Grenz, H.K. Eltzschig, Proc. Natl. Acad. Sci. U. S. A. 110 (2013) 18351–18352.
[36] S.P. Colgan, J. Invest. Med. 64 (2016) 364–368.
[37] E.A. Novak, K.P. Mollen, Front. Cell. Dev. Biol. 3 (2015).
[38] M.E.V. Johansson, J.K. Gustafsson, J. Holmén-Larsson, K.S. Jabbar, L. Xia, H. Xu, F. K. Ghishan, F.A. Carvalho, A.T. Gewirtz, H. Sjövall, G.C. Hansson, Gut 63 (2014) 281.
[39] S. Salim, J.D. Söderholm, Inflamm. Bowel Dis. 17 (2011) 362–381.
[40] H. Li, S. Cheng, J. Zhai, K. Lei, P. Zhou, K. Cai, J. Li, J. Mater. Chem. B 11 (2023) 8387–8403.
[41] S. Tsuda, J. Carreras, Y.Y. Kikuti, H. Nakae, M. Dekiden-Monma, J. Imai, K. Tsuruya, J. Nakamura, Y. Tsukune, T. Uchida, M. Matsushima, G. Roncador, T. Suzuki, N. Nakamura, T. Mine, Pathol. Int. 69 (2019) 260–271.
[42] D. Lissner, M. Schumann, A. Batra, L.-I. Kredel, A.A. Kühl, U. Erben, C. May, J.-D. Schulzke, B. Siegmund, Inflamm. Bowel Dis. 21 (2015) 1297–1305.
[43] B. Chami, N.J.J. Martin, J.M. Dennis, P.K. Witting, Arch. Biochem. Biophys. 645 (2018) 61–71.
[44] S.R. Sinha, Y. Haileselassie, L.P. Nguyen, C. Tropini, M. Wang, L.S. Becker, D. Sim, K. Jarr, E.T. Spear, G. Singh, H. Namkoong, K. Bittinger, M.A. Fischbach, J. L. Sonnenburg, A. Habtezion, Cell Host Microbe 27 (2020) 659–670. .e655.
[45] Y. Qu, C. Su, Q. Zhao, A. Shi, F. Zhao, L. Tang, D. Xu, Z. Xiang, Y. Wang, Y. Wang, J. Pan, Y. Yu, Front. Pharm. 13 (2022).
[46] J. Xie, L.-f Li, T.-y Dai, X. Qi, Y. Wang, T.-z Zheng, X.-y Gao, Y.-j Zhang, Y. Ai, L. Ma, S.-l Chang, F.-x Luo, Y. Tian, J. Sheng, Mol. Nutr. Food Res. 66 (2022) 2100408.
[47] J. Mu, C. Li, Y. Shi, G. Liu, J. Zou, D.-Y. Zhang, C. Jiang, X. Wang, L. He, P. Huang, Y. Yin, X. Chen, Nat. Commun. 13 (2022).
[48] T. Quach, M. Tippens, F. Szlam, R. Van Dyke, J.H. Levy, M. Csete, Liver Transpl. 10 (2004) 123–128.
[49] Y.J. Fu, X. Zhao, L.Y. Wang, K. Li, N. Jiang, S.T. Zhang, R.K. Wang, Y.F. Zhao, W. Yang, Adv. Mater. 36 (2024).